

Compactness Inference in Gravitational-Wave Mergers with PhenomDECO: Catalog Benchmarks and Robustness Diagnostics

Shrobona Ghosh,^{1,2,*} Charlie Hoy,^{3,†} Mark Hannam,⁴ and Frank Ohme^{1,2}

¹Max Planck Institute for Gravitational Physics (Albert Einstein Institute), Callinstrasse 38, D-30167 Hannover, Germany

²Leibniz University Hannover, 30167 Hannover, Germany

³Institute of Cosmology and Gravitation, University of Portsmouth, Portsmouth, PO1 3FX, UK

⁴Gravity Exploration Institute, Cardiff University, Cardiff, United Kingdom

Several gravitational wave (GW) observations have been identified as binary black hole (BBH) mergers, including systems with component masses that challenge typical formation scenarios. These observations motivate broader tests of whether the detected sources are consistent with this interpretation. We address this question using PhenomDECO, an existing phenomenological extension of a BBH model that uses an effective compactness parameter to characterize departures from the expected merger morphology. Applying this model to all high-significance BBH events from GWTC-3, we establish PhenomDECO as a robust test of the nature of compact binaries. In preliminary analyses we identify three recurring posterior morphologies: (i) near-Gaussian peaks consistent with the BBH expectation $C \sim 0.5$, seen in 60% of events; (ii) posteriors with additional high-compactness support ($C \geq 0.8$); and (iii) dominant low-compactness modes near $C \sim 0.15$ in $\sim 20\%$ of cases. For the latter, the low-compactness modes disappear when the data, especially from Livingston, are analyzed from a higher starting frequency, indicating sensitivity to low-frequency noise artefacts. We further use time–frequency residuals, computed after subtracting maximum-likelihood BBH and PhenomDECO waveforms from the strain data, to assess if the data is better described by a compactness-based deformation. With this analysis, we conclude that all of the GWTC-3 observations that we have considered are indeed consistent with BBH sources. The exception is the high-mass GW231123 signal, for which data from *both* detectors must be analyzed above 50Hz to remove a low-compactness mode. This study shows that low-frequency data treatment is crucial before attributing apparent deviations from BBH expectations to exotic physics, and provides a benchmark for compactness-based tests of merger morphology in current and future GW detections.

I. INTRODUCTION

The rapidly growing catalog of compact binary coalescences (CBCs) [1–5] has widened the possibility of investigating the nature of compact objects as a data-driven question. GWTC-3 reported nearly 90 CBC candidates, while the released O4 catalogs [6, 7] add nearly two hundred new candidates, bringing the number of reported detections to over ~ 300 . This growing sample has repeatedly revealed systems that challenge typical binary formation scenarios [8], such as GW190814 [9] and GW230529_181500 [10], and very massive binaries, such as GW190521 [11] and GW231123_135430 [12]; we hereafter refer to all events through their shortened GWYYMMDD notation, see the Appendix for their full names. Motivation for probing such outliers comes from the fact that compact objects are especially powerful probes of fundamental physics: they provide both a strong-field environment where departures from standard black hole (BH) and neutron star (NS) descriptions may become observationally relevant and, through GW emission, a direct messenger of those dynamics.

Studying compact binaries in the strong-field regime requires numerical relativity (NR), since the late inspiral, merger, and ringdown cannot be described reliably using weak-field or slow-motion approximations alone. Numerical simulations provide the fully nonlinear GR baseline against which small deviations must be identified, and they are essential for calibrating the phenomenological and effective-one-body waveform models used in GW parameter estima-

tion [13–27]. This is especially important when testing compact object nature: a genuine non-BBH effect may appear only as a subtle change in the accumulated inspiral phase, the merger morphology, or the remnant ringdown, and must be distinguished from waveform systematics and GR effects such as spin precession, higher modes, eccentricity. Numerical studies of exotic compact object mergers, including boson-star binaries, have begun to show explicitly how non-BBH signals can either hide within the BBH waveform manifold with biased parameters or produce clear residual structure [28, 29], underscoring the need for diagnostics that track deviations across the full inspiral-merger-ringdown (IMR) signal.

Current GW-based tests of the nature of compact objects primarily constrain deviations from the BBH hypothesis either through inspiral effects, such as modified phase evolution from tidal interactions and spin-induced multipolar structure, or through properties of the post-merger remnant such as the quasinormal mode (QNM) spectrum of the ringdown [30]. To the best of our knowledge, existing observational tests of exotic compact object (ECO) binaries have not yet directly targeted modifications to the merger morphology. As a first step in this direction Ref. [31] introduced the PhenomDECO model, which phenomenologically modifies the inspiral–merger transitions of a BBH waveform model (PhenomD) through a single effective compactness parameter, C_{eff} .

Ref. [31] demonstrated that, in controlled injections with signal-to-noise ratio (SNR) ~ 25 , the effective compactness parameter in PhenomDECO can be recovered with percent-level precision, and showed that the model can also be applied to real GW events. The natural next step is therefore to deploy this framework across a broad population of mergers and ask whether any events show evidence for non-BBH-like compactness. In this sense, PhenomDECO offers a new

* shrobona.ghosh@aei.mpg.de

† charlie.hoy@port.ac.uk

way of searching the catalog: not by targeting a specific exotic model, but by asking whether the merger morphology of any event departs systematically from the BBH expectation within this phenomenological parametrization. Applied at population scale, such an analysis opens up the possibility of identifying unusual mergers that would merit closer follow-up as candidate exotic binaries. It also reveals population-level features of the compactness distribution of astrophysical binaries, which we report in a companion *Letter* [32].

In addition to establishing the behaviour of PhenomDECO on observed BBH-like events, it is important to test whether the framework can recover genuinely non-BBH-like compactness in a realistic setting. We therefore complement the catalog analysis with binary neutron star (BNS) injections, which provide controlled signals with compactness values distinct from the BBH limit. These injections help us validate the ability of PhenomDECO in responding to departures from BBH merger morphology when present, and assess the limitations of such recovery in practice.

However, because the inferred compactness reflects a phenomenological deformation of the merger morphology, an apparent departure from the BBH expectation may arise not only from genuinely non-BBH structure, but also from waveform systematics, missing physics, or detector artefacts. Benchmarking the behaviour of PhenomDECO on real GW data is therefore essential before interpreting any merger as exotic. Motivated by this, we apply PhenomDECO to a subset of the mergers observed so far by the international GW detector network of LIGO-Virgo-Kagra (LVK) [33–41] and use the resulting population to establish an empirical baseline for BBH-like compactness posteriors. This baseline both reveals recurring posterior morphologies and systematic failure modes, and provides the context for the operational criteria defined in Sec. III B particularly the requirement that any apparent exclusion of the BBH value $C = 0.5$ remain stable under robustness tests. In this way, the catalog analysis serves not only as a search for candidate exotic mergers, but also as the empirical context needed to interpret effective compactness measurements on real GW data using PhenomDECO.

We describe a binary using its total mass $M = m_1 + m_2$, the mass ratio $q = m_2/m_1 \leq 1$, and the two spin combinations most relevant for the waveform morphology. The effective aligned spin is denoted by χ_{eff} , while the spin precession parameter is denoted by χ_p . In section II we place PhenomDECO in the context of complementary tests of exotic compact binaries and outline the analysis setup. Section III discusses the different types of effective compactness posterior we noted in the sample population, while Section IV presents the results across the sample, and a few special events from the fourth observing run (O4). Section V shows how residual diagnostics can further inform searches for exotic binaries.

II. TESTING THE NATURE OF COMPACT BINARIES

Testing the nature of compact objects in GW observations involves, in principle, testing the nature of three objects: the

two components of the binary and the remnant formed after merger. Existing tests broadly fall into two classes. The first targets the binary components during the inspiral, for example by allowing parametrized deviations in the waveform phase associated with finite-size effects such as spin-induced multipole moments [42–44]. The second targets the remnant, through BH spectroscopy with parametrized ringdown deviations [30, 45, 46] or through searches for post-merger echoes [47, 48]. These complementary tests face distinct challenges: during the inspiral, the phase is the primary accurately measurable quantity sensitive to the nature of the components, but it is also affected by many other physical effects and possible modelling systematics; in the ringdown and post-merger regime, the available SNR is typically lower, and conclusions can be sensitive to assumptions such as the ringdown start time.

The strength of the above approaches lies in the fact that their results can be interpreted in terms of specific physical effects tied either to the binary components or to the remnant. However, they probe only selected parts of the full coalescence signal. In particular, if deviations from the BBH signal are expected to become most prominent in the nonlinear merger regime, then purely inspiral-based or post-merger/ringdown-based tests may miss part of the relevant phenomenology. In addition, spin-induced multipole tests are most informative for binaries with appreciable component spins, which limits their applicability across the observed population. A full inspiral–merger–ringdown (IMR) test of ECO binaries, based on compactness as a generic property of compact objects, could therefore provide a useful probe of the strong-field merger regime while tracking deviations consistently across the full signal. A related class of tests is provided by IMR consistency tests (IMRCT) [49, 50], which check whether the weak-field inspiral and the strong-field merger–ringdown portions of the signal give mutually consistent source properties. These tests are powerful diagnostics of broad departures from the standard BBH description, including possible deviations from GR, non-BBH component structure, or other unmodelled physical effects. However, precisely because they are sensitive to many possible sources of inconsistency, their results are less directly interpretable as tests of compact object nature alone.

A. Compactness

Compactness is conventionally defined as $C := m/r$ in geometrized units, for an object of mass m and radius r . For a binary, one can analogously introduce a geometric compactness proxy by comparing the total mass to a characteristic length scale of the system close to merger. Taking this length scale to be set by the sum of the characteristic radii of the two objects gives

$$C_{\text{geometric}} = \frac{m_A + m_B}{r_A + r_B}, \quad (1)$$

where m_i and r_i denote the mass and characteristic radius of object ($i = A, B$), respectively. Noting that for a black hole,

$$r_i \equiv r_i^{\text{horizon}} = m_i + \sqrt{m_i^2 - a_i^2} = m_i \left(1 + \sqrt{1 - \chi_i^2}\right), \quad (2)$$

where a_i is the Kerr parameter ($|a_i| \leq m_i$) and $\chi_i = \frac{a_i}{m_i}$, is the dimensionless spin, we can rewrite Eq. (1) as,

$$C_{\text{geometric}} = \frac{m_A + m_B}{m_A \left(1 + \sqrt{1 - \chi_A^2}\right) + m_B \left(1 + \sqrt{1 - \chi_B^2}\right)}. \quad (3)$$

Written this way, it is easy to see $C_{\text{geometric}} \geq 0.5$ for astrophysical BHs with any combination of component masses and $|\chi_i| \leq 1$. For example, for $\chi_A = \chi_B = \chi$ it simplifies to $1/(1 + \sqrt{1 - \chi^2})$, yielding $C_{\text{geometric}} > 0.5$ for non-zero χ .

B. PhenomDECO: A Brief Recap

Lower compactness for the individual components imply larger objects and therefore an earlier onset of the post-contact stage of the signal. PhenomDECO is a modification of a standard aligned-spin BBH waveform model that adds an extra degree of freedom to PhenomD [15, 16], by taking the impact of lower compactness into account. Specifically, PhenomDECO allows the inspiral to terminate earlier than in the BBH case, before smoothly transitioning to a BBH-like continuation beyond that point. This continuation is not intended as a physical model of ECO post-contact dynamics, but as a phenomenological prescription that preserves continuity with the BBH limit. This choice reflects a broader limitation in the current literature: fully relativistic simulations of ECO mergers remain scarce, with boson-star binaries being one of the few cases studied in detail [28, 51–55]. While PhenomDECO can be generalized to include finite-size effects in the phase and post-contact/ringdown deviations, in its present form we focus on finite-size effects encoded only in the waveform amplitude morphology near merger.

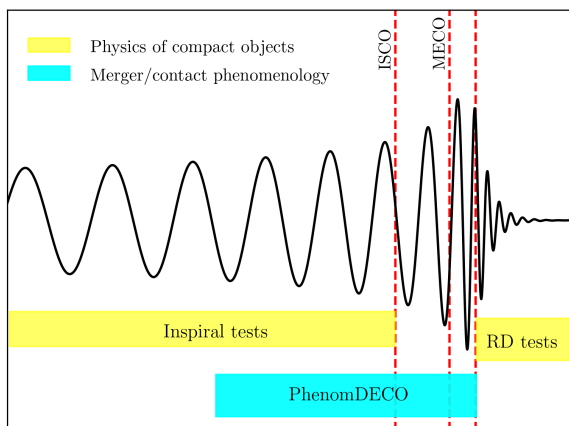


FIG. 1: The time domain GW signal associated with a BBH merger, with the binary mass scaled out, is shown in black; the characteristic dimensionless frequencies are indicated by dashed vertical lines. The tests that probe the physics of individual BHs are denoted in yellow (ringdown abbreviated as RD), while the test of merger phenomenology is indicated in cyan.

The amplitude morphology is modified through C_{eff} that controls the transition from inspiral to merger–ringdown according to how close the objects can approach at merger.

While this parameter is motivated by the same geometric intuition as $C_{\text{geometric}}$, the two quantities are not interchangeable. This is because PhenomDECO does not currently model spin dependence of the compactness parametrization self-consistently. Specifically, the present parametrization maps the inspiral–merger transition frequencies of all BBHs, independent of component masses or spins, to the geometric compactness of a nonspinning BBH, i.e., 0.5. By construction PhenomD already incorporates component spins aligned with the orbital angular momentum through a mass-weighted spin combination [14], but spin-dependent changes in $C_{\text{geometric}}$ are not mapped into the current parametrization. Including an explicit spin dependence in the compactness mapping may therefore improve the physical interpretation of inferred C_{eff} . Nevertheless, the central conclusion remains unchanged: within this parametrization, BBH-like configurations should not correspond to $C_{\text{eff}} < 0.5$. PhenomDECO should therefore be interpreted as a microphysics-agnostic probe of whether the merger morphology appears BBH-like, and only as an approximate measure of the objects’ compactness. In particular, a robust measure of $C_{\text{eff}} < 0.5$ does tell us that at least one of the objects is not a BH.

Figure 1 illustrates the stage of the binary coalescence at which PhenomDECO is most sensitive to departures from a standard BBH signal. Three characteristic frequencies are indicated in red: the orbital frequency at the innermost stable circular orbit (ISCO) of a non-spinning black hole with mass equal to the total binary mass, which is often used as a rough upper limit for the regime in which the post-Newtonian (PN) approximation remains reliable; the minimum-energy circular orbit (MECO) frequency, often a better proxy for the inspiral-to-plunge transition, especially for comparable-mass binaries; finally, the characteristic ringdown frequency of the remnant. As denoted on the figure, the inspiral-based tests of nature of components rely on the dephasing before ISCO, while ringdown-based tests track departures from a Kerr geometry of the remnant. PhenomDECO on the other hand probes the merger phenomenology through late-inspiral and merger/contact. It is complementary to existing tests in the part of the IMR signal it probes and allows us to test the nature of compact objects from a different angle: how BBH-like is the merger morphology of a GW observation? This immediately implies: (i) PhenomDECO would be generally more informative on deviations from BBH for shorter signals (i.e., higher-mass binaries), for which a larger fraction of the observed SNR lies near merger; and (ii) it can serve as a complementary cross-check to IMRCT, probing for tensions between the weak-field inspiral dynamics and the late-inspiral/merger waveform morphology, since it matches the corresponding BBH approximant exactly in the inspiral regime.

C. PhenomDECO waveform systematics

The baseline BBH model used in PhenomDECO does not include higher multipoles or precessional effects from in-plane spins. These missing effects can, in principle, introduce waveform-modelling systematics in effective compactness measurements. We distinguish here between two

possible effects: a direct degeneracy, in which precession produces an amplitude signature similar to the compactness-dependent modification targeted by PhenomDECO, and an indirect bias, in which precession biases the recovery of other BBH parameters that are correlated with compactness. The first possibility appears to be limited. This is illustrated using the frequency-domain amplitude of the standard precessing BBH waveform model PhenomXPHM [56]. As shown in the left panel of Fig. 2, the amplitude near merger exhibits very little sensitivity to precessing spins. This contrasts with the right panel, where aligned spin has a little more noticeable impact on the amplitude morphology. We therefore expect direct degeneracies between precession and effective compactness measurement to be limited.

We test this expectation with unequal-mass BBH injections with $q = 0.5$ and $M = 45 M_{\odot}$, generated with PhenomXPHM and recovered with PhenomDECO in a Bayesian analysis assuming advanced LIGO detector sensitivity [33]. As a control case, we first consider non-precessing injections with $\chi_{\text{eff}} = \{0.3, 0.6\}$ at SNR ~ 50 , shown in the left panel of Fig. 3. In these cases all parameters are well recovered, including the mass ratio, χ_{eff} , and effective compactness, with only mild degeneracies between χ_{eff} and effective compactness. The precessing injections, shown in the right panel of Fig. 3, illustrate the second effect; we inject signals with $\chi_p = \{0.2, 0.7\}$, moderate χ_{eff} , and SNR ~ 12 . In these cases, PhenomDECO recovers the signals with mild to moderate biases in χ_{eff} and larger departures from $C_{\text{eff}} = 0.5$; the bias persists even when we restrict to posterior samples with $C_{\text{eff}} = 0.5$, suggesting that the bias is not introduced by the compactness degree of freedom but instead reflects the recovery of precessing signals with an aligned-spin model. Given the mild correlation between χ_{eff} and effective compactness seen in the non-precessing injections, this suggests that the compactness bias may be driven, at least in part, by the biased recovery of χ_{eff} . However, these injections indicate that none of these systematics can mimic the low-compactness measure that we would classify as non-BBH. A non-BBH classification by PhenomDECO is therefore less directly exposed to the systematics that affect tests based on accumulated phase differences, such as dephasing caused by inaccuracies in, or omissions from, the modelling of various general relativistic (GR) effects. We discuss the systematic biases introduced by neglecting tidal effects in sec. IID.

The most prominent systematic we find with PhenomDECO is a degeneracy in the waveform for $C_{\text{eff}} \geq 0.5$. This is demonstrated in Fig. 4, where we show the time-domain behaviour of PhenomDECO for different values of the effective compactness. Since all waveforms share the same orbital parameters and differ only in C_{eff} , we impose a physically motivated alignment by requiring them to reach the starting frequency of 20 Hz at the same time. With this alignment, the waveforms for $C_{\text{eff}} > 0.5$ remain largely indistinguishable from the BBH case across the full inspiral–merger–ringdown signal, as shown in the top-right panel (see also Fig. 2 in Ref. [32]). By contrast, the $C_{\text{eff}} < 0.5$ waveforms cannot be aligned with the BBH waveform throughout the full signal. Instead, they exhibit the expected behaviour: the transition from inspiral to merger–ringdown occurs earlier and the

waveform is shorter, as illustrated by the lower panel of Fig. 4. The top left panel shows that these waveforms can be aligned in early inspiral. We therefore interpret support for $C_{\text{eff}} > 0.5$ to be consistent with BBH within this parametrization.

D. Impact of missing tidal effects on effective compactness inference

Since PhenomDECO is constructed as a phenomenological modification of a BBH baseline waveform, an important expected systematic in the recovery of C_{eff} is the absence of tidal effects. Such effects are generically expected for neutron stars and may also arise for other non-BBH compact objects, and can therefore bias the interpretation of the compactness inferred through Bayesian inference. We use BNS injections as a controlled stress test of this systematic. To ensure that the merger, where the PhenomDECO modification is most directly probed, remains visible in band, we perform these analyses using the Einstein Telescope sensitivity curve [57]. To sample the posterior distribution, we use *dynesty* [58] via *bilby* [59, 60], as has been done by the LVK consistently since the third GW observing run. To interface with PhenomDECO we use the modifications described in Ref. [31]. We also assume wide and agnostic priors following the conventions adopted by the LVK, *e.g.* we sample uniformly in component masses, and we use 2000 live points to improve sampler convergence.

We first analyze the BNS NR waveform BAM-0094 from the CoRe database [61], which contains only ~ 12 cycles before merger. As discussed in the *Letter* [32], this provides a clear validation case with PhenomDECO recovering a low effective compactness, $C_{\text{eff}} \approx 0.15$, and confidently excludes the BBH-like value $C_{\text{eff}} = 0.5$. The inferred compactness also agrees well with the approximate geometric estimate $C_{\text{geometric}}$. However, the same analysis shows significant biases in the recovered mass ratio and χ_{eff} , together with smaller biases in the chirp mass. To test whether these biases arise from the BBH baseline waveform rather than the compactness-based modification in PhenomDECO, we analyse a hybrid BNS waveform from the CoRe database [61], constructed by matching analytical inspiral predictions to the late-inspiral and merger portion of the NR simulation [62]. Although the hybridisation significantly increases the inspiral of the NR waveform, the starting frequency is ~ 200 Hz. We therefore only analyse data between $200 < f < 1680$ Hz. We find that the mass-ratio bias persists in the hybrid analysis, consistent with the findings of Ref. [62]. This supports the interpretation that the bias is driven by the baseline waveform model PhenomD.

The hybrid waveform analysis showed similar biases in the mass ratio, although the bias in χ_{eff} was reduced. However, unlike the NR case, the compactness posterior for the hybrid waveform prefers a BBH-like value. This is unexpected because the merger remains in band for both injections, and one might therefore expect the compactness information near merger to be recovered in both cases. We performed several diagnostic tests, including truncating the post-merger signal to one cycle after the peak, reducing the number of inspiral cycles (from 3000 cycles in the original hybrid signal), and restricting the set of parameters the likeli-

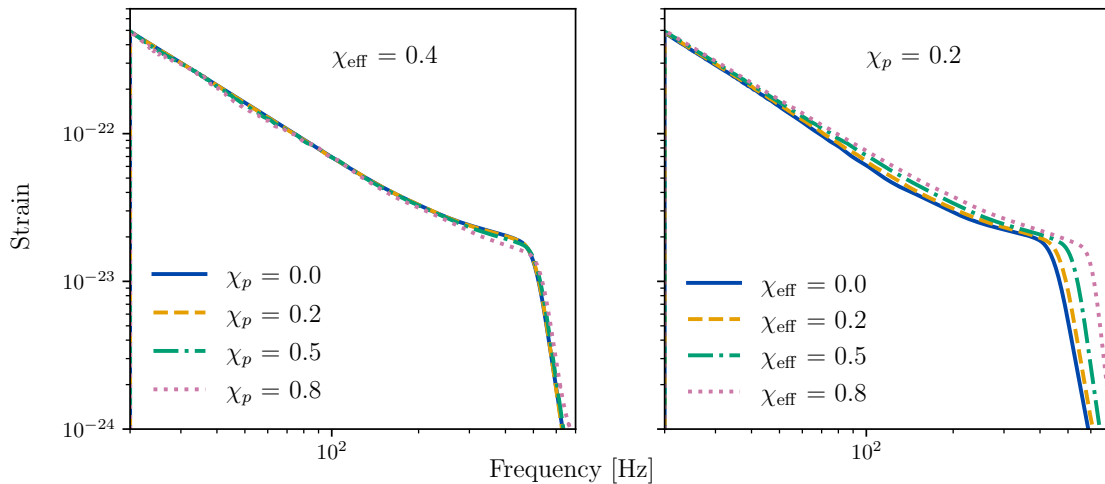


FIG. 2: Frequency-domain amplitude for precessing binaries generated with the standard precessing binary waveform model `PhenomXPHM` for an equal-mass binary with $M = 40 M_{\odot}$. The left panel shows waveforms with fixed $\chi_{\text{eff}} = 0.4$ and increasing precessing spin $\chi_p = \{0.0, 0.2, 0.5, 0.8\}$, shown with solid, dashed, dash-dotted, and dotted lines, respectively. The right panel shows waveforms with fixed $\chi_p = 0.2$ and increasing effective aligned spin $\chi_{\text{eff}} = \{0.0, 0.2, 0.5, 0.8\}$, shown with solid, dashed, dash-dotted, and dotted lines, respectively.

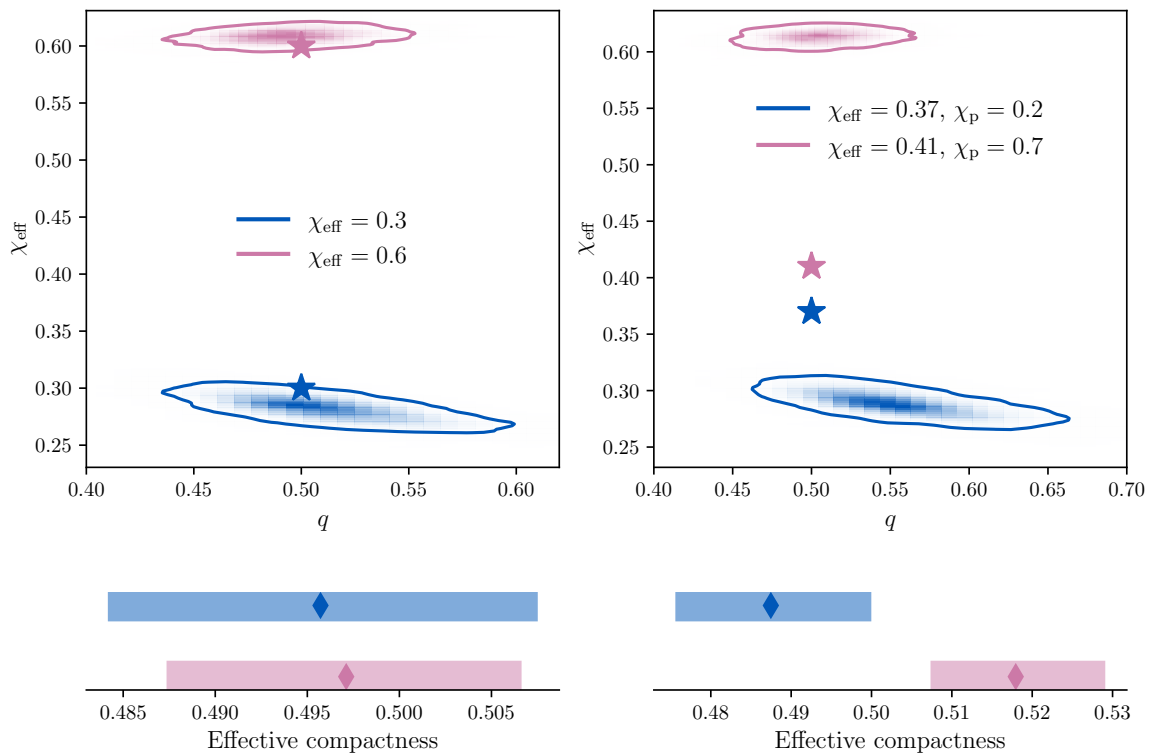


FIG. 3: Two-dimensional posterior probability distributions in mass ratio q and effective aligned spin χ_{eff} for unequal-mass BBH injections with $M = 45 M_{\odot}$ and $q = 0.5$. The left panel shows aligned-spin injections at $\text{SNR} \sim 50$, with $\chi_{\text{eff}} = 0.3$ shown in blue and $\chi_{\text{eff}} = 0.6$ shown in pink. The right panel shows precessing injections at $\text{SNR} \sim 12$, with $(\chi_{\text{eff}}, \chi_p) = (0.37, 0.2)$ shown in blue and $(\chi_{\text{eff}}, \chi_p) = (0.41, 0.7)$ shown in pink. In both panels, the injected values are marked by stars of corresponding colour. The lower subpanels show the corresponding effective compactness posteriors as horizontal box plots, with the marker indicating the median and the box edges enclosing the 90% CI. The precessing injections were performed at an orbital inclination $\theta_{\text{jn}} = 0.4$, to ensure precessional modulations were not suppressed.

hood samples over. A non-BBH compactness was recovered only in the restricted analysis where the likelihood sampled over just C_{eff} , geocentric trigger time, and luminosity dis-

tance while fixing all other intrinsic and extrinsic parameters, as shown in Fig. 5. Furthermore following a prescription similar to [32], we estimate a $C_{\text{geometric}} \simeq 0.15$ which is

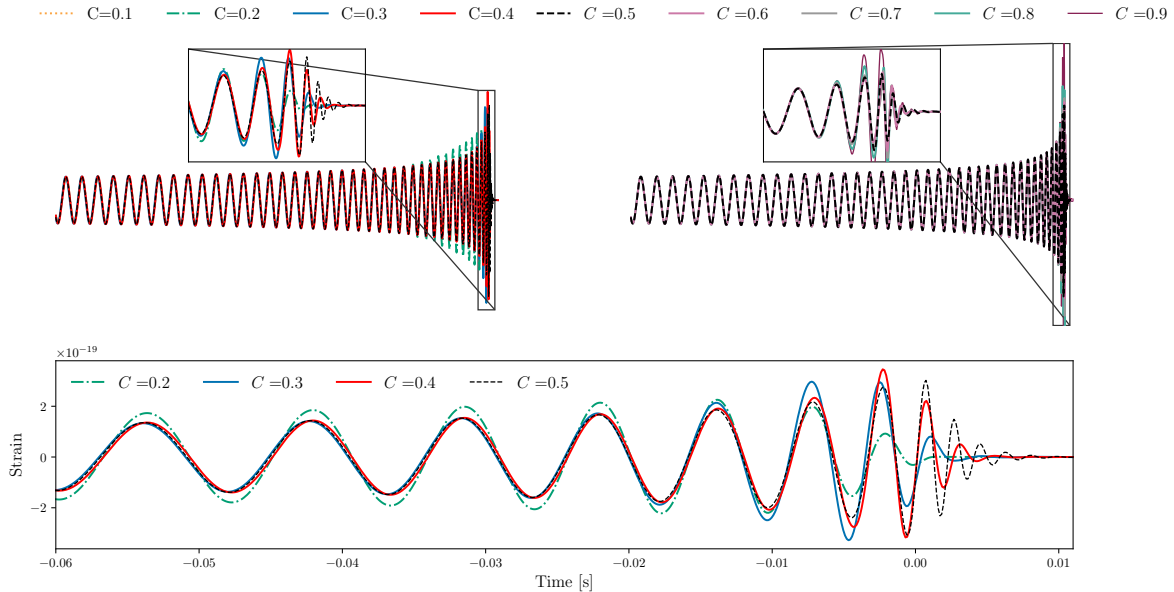


FIG. 4: Time-domain PhenomDECO waveforms for different values of the effective compactness $C_{\text{eff}} = [0.1, 0.2, 0.3, 0.4, 0.6, 0.7, 0.8, 0.9]$, for a fixed mass ratio of $q = 0.5$ and $M = 30M_{\odot}$. The top left panel shows waveforms with $C_{\text{eff}} < 0.5$, with the BBH expectation $C_{\text{eff}} = 0.5$ shown as a black dashed line. The top right panel shows that cases with $C_{\text{eff}} > 0.5$ are largely identical to the BBH waveform. The lower panel shows the last few cycles where the early end of inspiral based on compactness is easy to note. Signals with $C_{\text{eff}} < 0.2$ are significantly shorter and terminate earlier than the time window shown.

inconsistent with the inferred value even in the restricted likelihood analysis. This indicates that although its performance remains robust for transient signals, as demonstrated by the BNS NR injection discussed above, a prescription for tidal effects will be necessary before PhenomDECO can be reliably applied to long-duration signals.

III. BROAD TRENDS AND NON-BBH CLASSIFICATION

We perform Bayesian inference with PhenomDECO on all high-significance BBH events from GWTC-3, defined by a false-alarm rate $< 0.25 \text{ yr}^{-1}$, for a total of 69 events listed in Table III in Appendix A. As in Sec. IID, all Bayesian analyses are performed with *dynesty* via *bilby*. Throughout this and subsequent sections, we use the same priors and sampler settings as those done in the original LVK analysis unless otherwise stated. The only difference is that we project the priors into the non-precessing space, i.e. we marginalize over the in-plane spin directions, since PhenomDECO does not incorporate precession effects, and we use a uniform prior for the effective compactness over the interval $[0.1, 0.99]$.

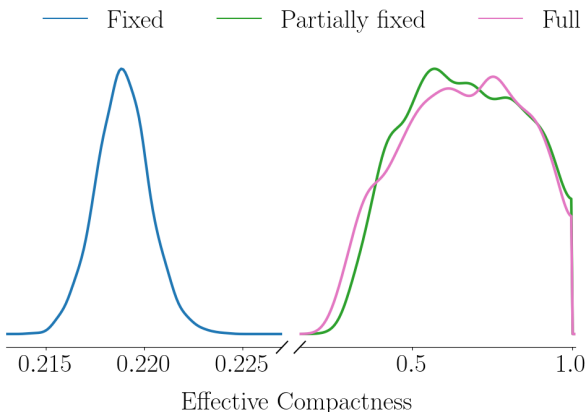


FIG. 5: The inferred effective compactness when analyzing an NR-hybrid waveform injected in ET. We show the posterior distribution obtained when using the full likelihood (pink), when fixing the chirp mass, total mass and mass ratio to their true values (green), and when fixing all parameters except for the luminosity distance, effective compactness and merger time (blue).

A. Trends in effective compactness posteriors

In this section, we summarize the trends observed in effective compactness posterior probability distributions from Bayesian inference across the events quoted above. Under the approximation adopted in PhenomDECO, $C_{\text{eff}} = 0.5$ represents the reference BBH limit. BBH-like events are therefore expected to remain consistent with this value, although waveform systematics and noise fluctuations can mildly displace the peak below 0.5 or introduce additional support at $C_{\text{eff}} \geq 0.5$, as discussed in Sec. IVC3. The studies in Sec. II suggest that precession can produce small downward shifts in the inferred compactness for BBH signals, even in the absence of noise. However, the observed shifts are not large enough to account for the low-compactness departures

considered here, such as $C_{\text{eff}} \leq 0.4$. This underscores the scope of PhenomDECO : *it is best suited to identify candidate ECO binaries with effective compactness significantly below the BBH limit*. We find three broad trends across the full set of events that we discuss below.

1. Dominant peak near $C=0.5$

About two thirds of the events show posteriors consistent with BBH, which we classify as typical behaviour. As shown in Figure 6, this category includes posteriors that: (i) exhibit a clear peak near $C = 0.5$ (GW190731); (ii) peak at 0.5, but with a very broad 90% credible interval (CI) (GW170608); (iii) are bimodal, with peaks displaced from $C = 0.5$ but including it well within the 90% CI (GW190620); and (iv) have a lower 90% CI bound only marginally above 0.5 (GW170814) as this kind of behaviour can happen due to missing physics (cf. Fig. 3). For these events, the inference on all other intrinsic parameters were found to be consistent with that reported in GWTC-3.

2. Support for $C > 0.5$

We found significant support for a compactness much higher than 0.5 for about ten events. Only one event shows a clear preference for $C \sim 0.9$ (GW170818), and in two other events $C = 0.5$ is excluded at 90% lower CI. In all the other cases, although the posterior probability favours a higher compactness, $C = 0.5$ was always included in the 90% CI, as shown in Fig. 6. We do not observe biases in the other inferred parameters for these events, nor do we find correlations with quantities such as q or χ_{eff} that would explain the preference for higher compactness. Likewise, neither the total mass nor the SNR of these events provides additional insight into their anomalous behaviour. Given these observations, together with the discussion on systematics of effective compactness in Sec. II, we interpret this behaviour as BBH-like rather than as evidence for exotic physics.

3. Spuriously low measure of compactness

Nominally, a compactness posterior whose upper 90% CI lies below 0.5 would suggest that one or both components are of exotic origin. However, as discussed above, modest downward deviations from 0.5 can arise for a variety of non-exotic reasons. We therefore regard a compactness posterior as potentially suggestive of non-BBH structure only when both the posterior peak and the upper edge of the 90% CI lie below $C \approx 0.4$. We note that none of the events in our study exhibited this behaviour.

The events considered in this subsection fall into a different category. In the initial analyses, roughly a dozen events showed a sharp low-compactness (low-C) mode near $C \sim 0.14 - 0.17$, excluding the BBH value at 90% upper CI. However, these runs failed to identify the signal at the known geocentric coalescence time, accompanied by inconsistent chirp mass recovery and biases in other parameters. These

pathological signatures are sufficiently pronounced to make the corresponding compactness measurements unreliable. The low-C modes are therefore best interpreted as arising from an interplay between the sampler and a short-duration burst of power near the signal, rather than as evidence for anomalously low compactness in the astrophysical source.

The events do not cluster in any particular region of the $\mathcal{M}\text{-}\chi_{\text{eff}}$ parameter space, nor did we find any clear trend with their SNR, suggesting that the failure mode is not simply associated with intrinsic source parameters or low-SNR events. The only event in this set known to be associated with data-quality issues is the precessing BBH GW200129 [63, 64]. However, we verified that this issue is unlikely to explain the anomalous compactness recovery, since the coalescence time preferred by PhenomDECO lies approximately 2s after the known coalescence time.

Another feature emerged from analyses of individual-detector data restricted to different frequency bands. Across a series of tests, we found that the anomalous low-C inference were primarily driven by the low-frequency content of the Livingston data. We note that low-frequency scattered-light noise in Livingston during O3, particularly in the 10–40Hz band, has also recently been discussed in Ref. [65]. While we do not attempt to identify a specific noise artefact in each event, this provides useful context for why the Livingston low-frequency data may be especially susceptible to this failure mode.

Figure 7 shows that for GW200224 [1], the inferred effective compactness varies significantly as a function of frequency. If the low-C was truly astrophysical, we would expect the compactness measurement to be independent of the frequency content included. Specifically, when using $f_{\text{low}} \geq 40$ Hz in the Livingston detector, we obtain a BBH like compactness. We also recover a chirp mass distribution comparable to that in the LVK analysis with PhenomXPHM. Repeating this analysis for the other affected events showed that the cutoff required to recover the correct signal varied from event to event. Nevertheless, using $f_{\text{low}} = 50$ Hz for the Livingston data alone removed the low-C peak in all cases and restored typical behaviour, as shown in the right panel of Fig. 6. This strongly refutes an astrophysical origin for these anomalies; we therefore use posterior samples from the analysis that uses Livingston data above 50 Hz for the rest of the paper.

B. Exotic binary characterisation with PhenomDECO

We define here the criteria for a binary to be labelled exotic from the results of Bayesian inference with PhenomDECO. These criteria are constructed to reflect the scope of the model, potential systematic biases in compactness inference arising from the omission of known physical effects, and susceptibility to noise artefacts:

- multidetector event
- $M > 10M_{\odot}$ to ensure that the transition to merger lies within the sensitivity of current LVK detectors;
- the effective compactness posterior excludes the BBH value $C = 0.5$ from its 90% CI, with the posterior support lying predominantly at $C < 0.5$;

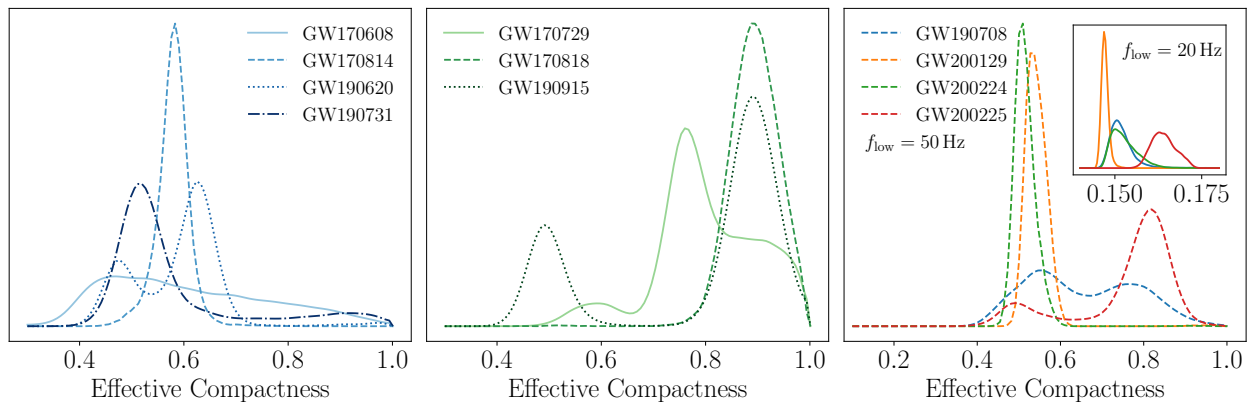


FIG. 6: Plot showing the inferred compactness for events that show *Left*: typical behaviour (defined in text); *Middle*: significant support above $C > 0.5$; *Right*: a clear preference for $C \sim 0.15$ when analysing data with frequencies > 20 Hz, but negligible support for $C < 0.5$ when analysing data with frequencies > 50 Hz in Livingston. In the *Right* panel, we explicitly show the posterior distribution obtained when consistently using a low-frequency cutoff of 20 Hz in all detectors in the inset, and the dashed lines show the posteriors obtained when analyzing Livingston data above 50 Hz and Hanford (and Virgo, where available) from the usual 20 Hz.

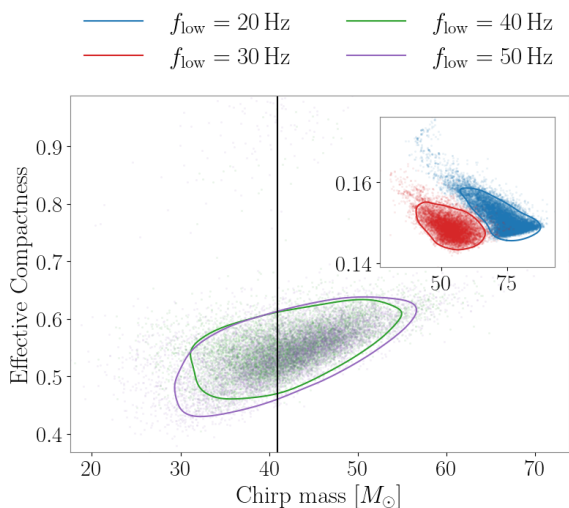


FIG. 7: Plot showing the 2D marginalized posterior distribution for the chirp-mass and effective compactness when analysing GW200224 with progressively higher low-frequency cutoffs in the Livingston detector, $f_{\text{low}} = [20, 30, 40, 50]$ Hz; we consistently used $f_{\text{low}} = 20$ Hz in the Hanford detector. The solid black vertical line shows the median chirp-mass inferred with `PhenomXPHM` by the LVK, and we obtain consistent results with $f_{\text{low}} = 40$ Hz. This is also the cutoff frequency at which the compactness posterior becomes consistent with BBH-like behavior. The inset shows a zoomed in region of the parameter space, focusing on $C \sim 0.15$.

- this exclusion of $C = 0.5$ persists under robustness tests in which the lower analysis frequency is varied over $f_{\text{low}} \in [20, 50]$ Hz in each detector;
- cases in which the posterior excludes $C = 0.5$ only in favour of $C > 0.5$ are not classified as exotic, since $C > 0.5$ is interpreted as BBH-like behaviour within the present parametrization rather than as a physical

compactness.

It is worth noting that the choice of the frequency range for criterion 4 is heuristic, based on current understanding of data quality. As we discuss in section IV C this condition may need to be revisited as our understanding of low-frequency detector artefacts and data quality evolves.

IV. RESULTS

Figure 8 summarizes the effective compactness posteriors for the full set of analyzed GWTC-3 events. The overall distribution shows a preference for BBH-like compactness values close to $C \simeq 0.5$, and no event satisfies the non-BBH classification criteria defined in Sec. III B. We note a general preference for compactness close to 0.5. However, a robust population-level constraint requires hierarchical inference, which we present elsewhere [32]. In this section, we discuss the effective compactness estimates for several notable events. We first consider unequal-mass binaries, for which shorter merger morphology of a low-compactness signal could in principle be partially mimicked by biases in the total mass or mass ratio. We also examine a couple of notable O4 events like GW250114 [66], selected for of its high SNR, and GW231123 due to its unusually high mass. We discuss GW231123 [12] separately, as its short in-band duration, and challenging waveform systematics make it a natural target for exploring alternatives to a standard BBH interpretation.

A. Unequal mass binaries

Reference [31] showed that, when ECO signals are characterized by an earlier end to the inspiral, they can be recovered by BBH templates with more asymmetric mass ratios. Events with large inferred mass ratios are therefore most likely candidates for mischaracterisation as ECO binaries

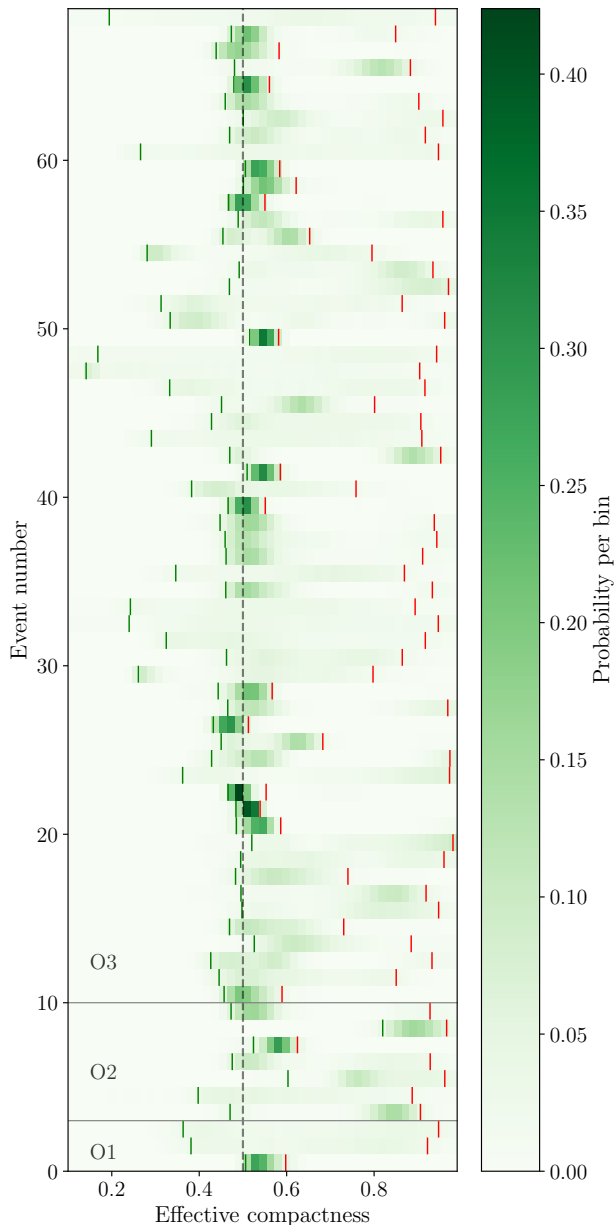


FIG. 8: Compactness posterior distributions for the analyzed GWTC-3 events, shown as normalized probability per bin on a common set of effective compactness bins. Each row corresponds to one event, indexed as listed in Table III of Appendix A, and the color indicates the normalized posterior probability in each bin. Darker regions indicate more sharply peaked compactness support, while lighter regions indicate broader or less localized posteriors. The grey vertical dashed line marks the BBH reference value $C_{\text{eff}} = 0.5$. For each event, the lower and upper bounds of the 90% CI are indicated by green and red vertical bars, respectively. Events that initially showed a sharp low- C mode near $C_{\text{eff}} \approx 0.15$ are shown here after reanalysing with a low-frequency cutoff of 50 Hz in Livingston data; in all the cases, the low- C support is removed and the posterior becomes consistent with BBH-like compactness. Notably, since none of the upper 90% CI lie below $C_{\text{eff}} = 0.5$, all analyzed events remain consistent with a BBH classification under our criteria.

within this framework. GW190412 [67] and GW190814 are significantly unequal in masses with $q \sim 0.3$ and $q \sim 0.1$, respectively and therefore plausible candidates for such mischaracterisation. However, with PhenomDECO we find them both to be consistent with BBH: GW190814 shows a single peak at $C \sim 0.53$, while the compactness posterior is bimodal and broad for GW190412, with a secondary peak at $C \sim 0.8$ (aside from the primary peak at $C \sim 0.5$). This is consistent with a bimodal distribution of mass ratio for this event. For both events, the recovered mass ratio is consistent with the corresponding BBH analyses, despite the fact that PhenomD (and therefore, PhenomDECO) does not include higher multipoles. Taken together with the broader event sample, these cases provide no evidence for a clear trend in which mass-ratio effects alone drive significant displacements of the compactness posterior away from $C \approx 0.5$.

B. Events from O4

For this first study, where we establish our methods, we have chosen to focus on GWTC-3, and will consider the complete set of published observations in future work. However, we do analyze a couple of O4 events that are of particular interest because of high SNR or unusual source properties.

GW250114 is the loudest GW event observed to date, with a network SNR of ~ 80 . The loudness of the event makes it a particularly valuable target for searches for departures from the BBH expectation; indeed, it has already been used for precision tests of GR and BH spectroscopy [68–70], all of which find consistency with GR predictions. For GW250114, we find that the low-compactness mode seen in some GWTC-3 events also appears when analysing the Livingston data from the standard low-frequency cutoff. Its recurrence in such a high-SNR event reinforces that this failure mode is not simply a consequence of low signal strength. As in the GWTC-3 cases, raising the Livingston low-frequency cutoff to 50 Hz removes the low-compactness support and recovers BBH-like behaviour, with $C_{\text{eff}} \sim 0.52^{+0.01}_{-0.01}$ at 90% CI.

Figure 9 places this final BBH-like posterior in context by comparing GW250114 with GW150914, a similar but much lower-SNR event. The comparison shows that the loudness of GW250114 substantially improves the compactness constraint (just as other parameters e.g. chirp mass), not only by narrowing the posterior but also by shifting its peak closer to the expected BBH value, $C_{\text{eff}} \approx 0.5$. The small residual offset from $C_{\text{eff}} = 0.5$ suggests that some further calibration of the phenomenological compactness mapping may be required to recover the BBH limit without bias. However, given the precision with which the merger morphology is measured, the complete absence of support at $C_{\text{eff}} < 0.5$ places an extremely strong constraint on the BH nature of GW250114, and also illustrates our ability to constrain compactness with even a simple phenomenological treatment.

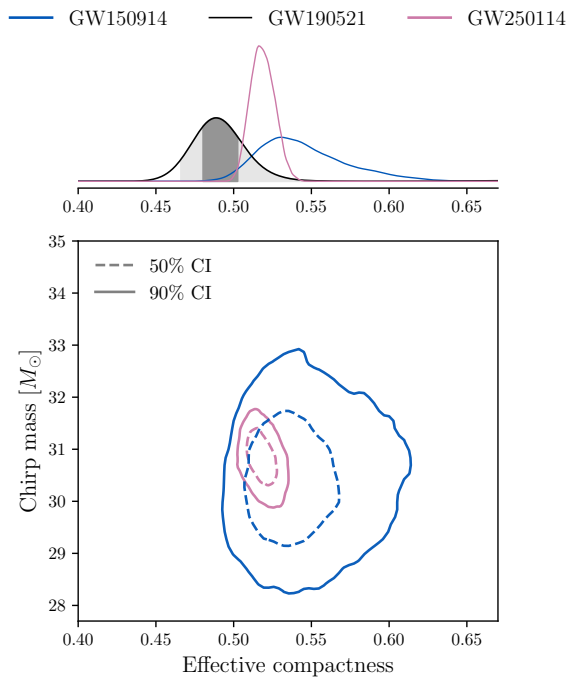


FIG. 9: The lower panel shows the two-dimensional posterior distributions for GW150914, in blue, and GW250114, in pink. Solid contours denote the 90% CI, while dashed contours denote the 50% CI. Although the two events are otherwise very similar, the higher SNR of GW250114 yields substantially tighter posteriors and shifts the posterior peak toward $C_{\text{eff}} \sim 0.5$. The upper panel shows the one-dimensional posterior on effective compactness. For comparison, we include GW190521, which provided the best-constrained effective-compactness posterior in GWTC-3, with an SNR ~ 15 . The dark shaded region marks the 50% CI and the lighter shaded region marks the 90% CI. The full one-dimensional posteriors for GW250114 and GW150914 are also shown for comparison.

C. GW231123 - a special case

1. Event properties and analysis challenges

We consider here the inference of source properties of GW231123 with PhenomDECO. This event is the most massive BBH system observed to date by the LVK and was detected by the LIGO Livingston and Hanford observatories. Because of the binary's short in-band duration, the detected signal is dominated by the merger-ringdown phase, with only a very brief inspiral contribution. The data from both detectors were also affected by non-Gaussian noise transients at times close to the merger signal [12]. Data-quality studies found that the transient in the Livingston data had no measurable impact on parameter estimation. However, glitches occurring in the temporal vicinity of the event in the Hanford detector may complicate the accurate inference of the source properties.

Aside from the large total mass, this event was also reported with a large component of misaligned spin, making it particularly challenging for state-of-the-art waveform ap-

proximants to converge on the source parameters. In fact it was demonstrated [12, 71] that similar systematics across waveform approximants could be reproduced even in the absence of noise, of course different noise realizations had different degree of impact on model systematics.

2. Effective compactness inference

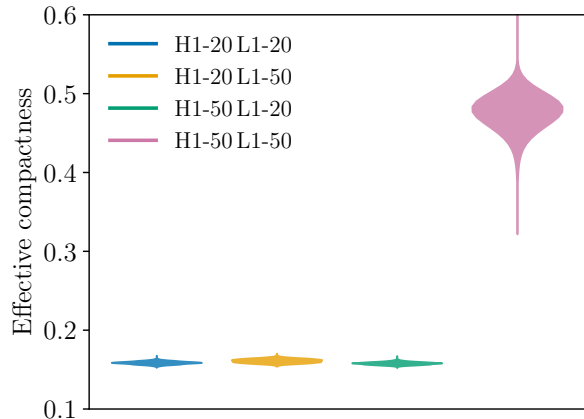


FIG. 10: Effective compactness inference for GW231123 using data above 20 Hz in both Livingston and Hanford is shown in blue. Raising the low-frequency cutoff to 50 Hz in either detector, while keeping the other at 20 Hz, leaves the compactness posterior largely unchanged, as shown in orange and green. A compactness posterior consistent with BBH, shown in pink, is recovered only when the low-frequency cutoff is set to 50 Hz in both detectors.

The application of PhenomDECO to the real GW231123 data produced an unexpected sequence of results. In the first three analysis configurations—using data above 20 Hz in both detectors, or raising the low-frequency cutoff to 50 Hz in only one detector at a time—the effective-compactness posterior showed pathologies similar to noted earlier in the low-compactness failure modes identified in the GWTC-3 sample. This motivated a final robustness test in which both Hanford and Livingston data were analysed only above 50 Hz. As shown in Fig 10, only for the final analysis do we recover a compactness consistent with expectations for BBHs and comparable to the compactness distribution inferred from GWTC-3. This behaviour differs from the low-compactness cases identified in GWTC-3, where raising the low-frequency cutoff in Livingston alone was sufficient to restore BBH-like compactness. For GW231123, the persistence of the low- C mode under single-detector cutoff changes indicates that the effect is not isolated to one detector in the same way.

Figure 11 compares the posterior distributions for the total mass, mass ratio, and effective spin inferred with PhenomDECO against the median of combined posteriors across several analyses reported in [12]. Among these, the analysis using a 50 Hz low-frequency cutoff gives estimates that are most consistent with those reported in [12].

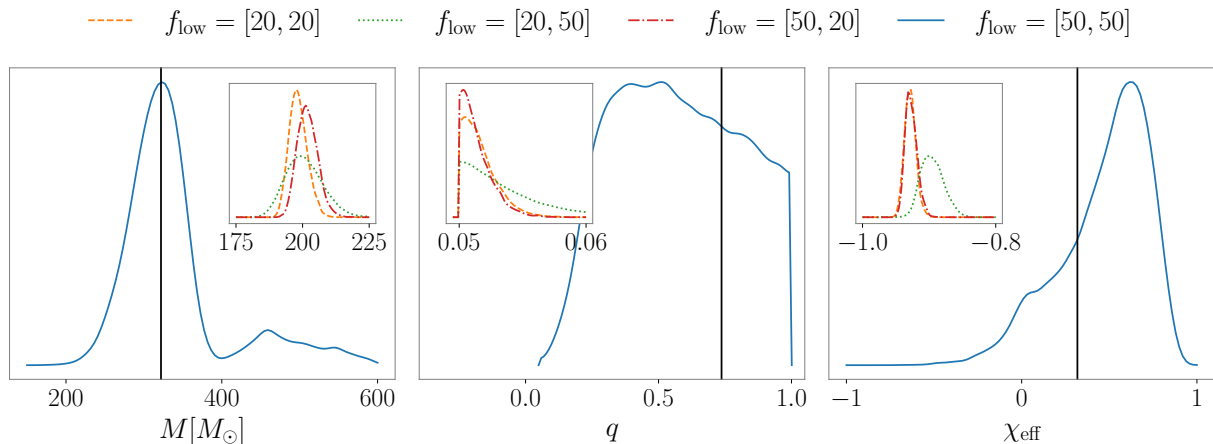


FIG. 11: Posterior probability distributions for the total mass (*Left*), mass ratio (*Middle*), and effective spin (*Right*), obtained when analyzing GW231123 with different low-frequency cut-offs in the Hanford and Livingston detectors. The solid vertical lines indicate the median values of the combined posterior distributions obtained in the LVK analysis, as reported in [12]. The insets in all panels show a zoomed in region of the parameter space.

3. PhenomDECO at high masses

The data-quality complications discussed in Sec. IV C 1, together with the modified frequency treatment required in Sec. IV C 2 to obtain non-pathological inference with PhenomDECO, motivate a closer examination of the model in this regime. We therefore verify that PhenomDECO can robustly infer source parameters for very high-mass, short-duration systems, including cases with significant spin precession. The short in-band duration of very massive binaries raises an important concern for PhenomDECO inference in assigning low effective compactness simply because the model can make the waveform shorter by shifting the IMR transitions to lower frequencies. In this case, an apparent low-compactness posterior would not reflect non-BBH merger morphology, but rather a failure mode of the parametrization in the high-mass regime. We first test this possibility with a high-mass nonspinning BBH injection generated using PhenomD and recovered with PhenomDECO in zero noise, which isolates the effect of total mass and signal duration from additional complications such as spin precession. In these control cases, PhenomDECO recovers the injected source parameters and returns compactness posteriors consistent with the BBH expectation, indicating that high total mass alone does not generically produce a spurious low-compactness measurement.

We then repeat the test with a more challenging injection designed to resemble GW231123. Specifically, we inject a PhenomXPHM waveform in zero noise at SNR ~ 26 , using the upper limits on the inferred component masses and the median values of $(\chi_{\text{eff}}, \chi_p, D_L, \theta_{jn})$ where D_L and θ_{jn} are the luminosity distance and inclination to source, respectively. Despite the short duration and the large misaligned-spin component, PhenomDECO again recovers the source parameters and yields an effective compactness consistent with the BBH value. Figure 12 shows the recovery for this injection, along with the nonspinning high-mass BBH injection and, neither of them show noticeable biases in the recov-

ered M , q or C_{eff} . $\chi_{\text{eff}} = 0.34$ is excluded at the 90% CI, consistent with biases in χ_{eff} seen for precessing systems with PhenomDECO (cf. fig. 3). These injection studies therefore indicate that neither high mass nor misaligned spin drives PhenomDECO toward a spurious low-compactness posterior, either individually or in combination, at least in the absence of detector noise.

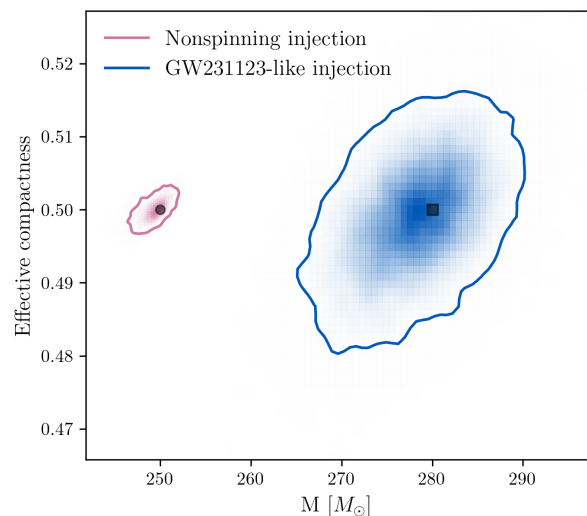


FIG. 12: Two-dimensional posterior distributions in total mass and effective compactness for high-mass BBH injections recovered with PhenomDECO. The pink contour shows the 90% credible region for a high-mass nonspinning control injection with $M = 250 M_{\odot}$, while the blue contour shows the corresponding region for a high mass precessing injection with $M = 280 M_{\odot}$. The injected values, with effective compactness fixed to the BBH value $C_{\text{eff}} = 0.5$, are indicated by a solid circle (square) for the nonspinning (precessing) injections. While $\chi_{\text{eff}} = 0$ is recovered well in the nonspinning case, the injected $\chi_{\text{eff}} = 0.34$ is completely excluded at 90% CI in the precessing case, without noticeable biases in mass ratio for either case.

Additionally, we analyzed another short duration event, GW190521, that has been considered for several different exotic scenarios and found PhenomDECO to favour a BBH classification. In fact, GW190521 yields the tightest constraint on compactness parameter across GWTC-3 with a clear preference for BBH, as depicted in the top panel of figure 9. Notably, despite the lower SNR of this event (~ 15) compared to GW231123 (~ 21), we did not need to employ any non-standard settings in bayesian inference to recover a compactness consistent with BBH. This suggests that high total mass and large component of misaligned spin do not inherently preclude a BBH characterization using effective-compactness inference with PhenomDECO on real detector data.

4. Interpretation

Within our analysis, GW231123 stands out as a special case in that a BBH-like characterization with PhenomDECO is obtained only after raising the low-frequency cutoff consistently in both detectors. Ordinarily, the persistence of a low-compactness mode under single-detector cutoff tests would make the event more suggestive of genuine non-BBH structure. However, GW231123 requires a more nuanced interpretation. Although the BBH-like result is recovered only with a modified low-frequency treatment, the analysis configurations that favour non-BBH compactness exhibit clear pathological behaviour. We therefore regard the BBH-like characterization as the most reliable among the runs considered here,

The BBH interpretation of GW231123 should nevertheless be caveated. As discussed above, PhenomDECO is designed to probe departures from BBH morphology primarily through the late-inspiral and merger transition. The interpretation of the compactness posterior therefore depends on whether this part of the waveform carries appreciable information in the data. Since the observed signal contains only about three cycles, the analysis may be driven either by late-inspiral/merger morphology or predominantly by ringdown. If sufficient late-inspiral and merger information remains in the data, then the recovery of BBH-like compactness when both detectors are analysed above 50 Hz provides meaningful support for a BBH-like merger morphology with PhenomDECO.

On the other hand, if the observation is effectively dominated by ringdown alone, then a BBH-like characterization with PhenomDECO is less informative. The present version of PhenomDECO does not model an exotic post-merger signal; after the compactness-dependent inspiral–merger modification, it continues with a BBH-like ringdown. A model whose ringdown is always BH-like can therefore fit a BH remnant efficiently even if the components were not BHs. Nevertheless, this does not make the compactness result completely arbitrary. For a genuinely low-compactness binary that promptly forms a BH remnant, the lower compactness would shift the merger/contact scale to lower frequencies; matching the observed frequency content would generally require different source parameters, in particular a substantially larger total mass of the binary, which would then change the expected remnant ringdown frequency. The

fact that the BBH-like PhenomDECO analysis recovers source properties broadly consistent with BBH analyses therefore gives some support to the standard interpretation, although it should not be read as a definitive exclusion of exotic scenarios.

Additionally, the absence of flagged coincident data-quality issues, together with the fact that the anomaly depends on a common low-frequency cutoff across detectors, makes a purely uncorrelated detector-noise explanation less compelling than in the GWTC-3 cases. Our analysis with GW231123 therefore motivates targeted follow-up studies of shared low-frequency systematics, glitch mitigation, and non-CBC transient models before any non-standard astrophysical interpretation can be drawn.

V. WAVEFORM SUBTRACTION AND RESIDUAL DIAGNOSTICS

The compactness posterior identifies events for which the data prefer merger morphologies away from the BBH expectation within the PhenomDECO parametrization. A complementary question is whether the waveform associated with the inferred compactness leaves residual structure in the data that is meaningfully different from that left by a standard BBH waveform. Residual-based diagnostics have also been proposed as a way to search for unmodeled physics in GW data: for example, the SCoRe framework looks for structured correlations in residual strain between detector pairs in order to distinguish noise artefacts from possible unmodeled signal components [72]. In this section we therefore compare time–frequency residuals obtained after subtracting the maximum-likelihood PhenomDECO and BBH waveforms from the detector strain. This diagnostic is not intended as a detection statistic, an evidence calculation, or a replacement for Bayesian model selection, but rather as a complementary robustness check. A Bayes factor between BBH and PhenomDECO would be sensitive to the prior volume assigned to the phenomenological compactness parameter, including regions that do not yield a significant likelihood improvement over the BBH model and therefore contribute to the Occam penalty [73]. The residual comparison avoids this particular dependence on the compactness prior by conditioning on the maximum-likelihood BBH and PhenomDECO waveforms and comparing the residual time–frequency power left by each subtraction.

For a given analysis, we construct residual data by subtracting a detector-projected maximum-likelihood waveform from the publicly released calibrated strain. Specifically, for each detector, we take the maximum-likelihood waveform from the Bayesian analysis, project it onto the detector response, and construct the corresponding signal time series. We then place this signal on the same time grid as the publicly available strain time series and subtract it sample by sample from the detector strain [30]. We repeat this procedure for both the baseline BBH waveform and PhenomDECO, thereby obtaining two residual time series for direct comparison.

A. Residual contrast as a detector-level diagnostic

To assess the remaining time-frequency structure, we examine the Q-transform spectrogram of each residual [74]. The data are first whitened using the detector noise power spectral density estimated from data segments excluding the chirp signal. We then use the `q_transform` method implemented in `gwpy` for `TimeSeries` objects [75] to project it onto time-frequency tiles with varying duration and bandwidth. This spectrogram is computed over a fixed window of ± 0.4 s around the merger time and over the frequency band 20–500 Hz. The normalized energy shown in the spectrogram measures the excess power in each tile relative to the local noise expectation.

Localized transient excess power is captured by a relatively small subset of time–frequency tiles with large normalized energy, whereas stationary noise is distributed more broadly across the tiling. Therefore, summing the normalized energies of tiles above a threshold provides a simple measure of the localized residual structure left after subtraction. Motivated by this, we define, for each detector separately, a diagnostic—*residual contrast*—that compares the residuals obtained from the two waveform models, as

$$\Delta_{\text{res}}(\tau) = \left| \frac{\sum_{i \in \tau} E_i^{\text{BBH}} - \sum_{i \in \tau} E_i^{\text{PhenomDECO}}}{\sum_{i \in \tau} E_i^{\text{strain}}} \right|, \quad (4)$$

where $E_i^{\text{BBH}/\text{PhenomDECO}}$ is the normalized energy in i^{th} tile of the residual spectrogram, E_i^{strain} is the normalized energy in the i^{th} tile of the original strain data, and the summation is carried out over tiles with normalized energy above the chosen threshold, τ . We use Δ_{res} only as an event-level diagnostic, not as a detection statistic or cross-event ranking. It measures whether the BBH waveform and PhenomDECO maximum-likelihood subtractions leave comparable localized excess power in a given detector. Because the normalization is detector-specific, values should not be compared directly across events. We report the residual contrast for a subset of events in Table I and discuss three representative cases below to illustrate its interpretation.

TABLE I: Detector-level residual contrasts for selected events shown for a choice of threshold on normalized energies, only for the Livingston detector (LLO)

Event	Detector	Threshold	Residual contrast
GW150914	LLO	10	0.028
GW170608	LLO	10	0.013
GW170729	LLO	10	0.012
GW190408	LLO	10	0.016
GW190412	LLO	10	0.013
GW190915	LLO	10	0.024
GW200129	LLO	10	0.017
GW19112	LLO	10	0.037
GW200219	LLO	10	0.077

1. GW200129

First, we consider GW200129 which is one of the events where we found a spurious low-compactness peak at ~ 0.15 .

Using a low frequency cutoff of 50 Hz for Livingston data, while keeping 20 Hz for Hanford, shifts the recovered compactness posterior to a peak near 0.5. The associated spectrograms are consistent with this behaviour: the maximum-likelihood waveform from the analysis yielding the BBH-like compactness posterior leads to a clean subtraction and similar residual features as the standard BBH waveform (PhenomXPHM), as shown in Fig. 13 This provides an example where the compactness inference can be misleading if considered without residual diagnostics. In the nominal analysis, the compactness posterior develops a pronounced peak near $C \sim 0.15$, with no support in posterior probability distribution for $C = 0.5$. In keeping with the erroneous geocentric trigger time, inspection of the residual spectrogram also shows that this low-compactness solution does not correspond to a clean subtraction of the chirp signal. When the analysis is repeated after excluding data below 50 Hz in the Livingston detector, the compactness posterior shifts back to a BBH-like value near $C \sim 0.5$, and the corresponding residual spectrogram is much cleaner. This behaviour corroborates that the original low-compactness peak was spurious and driven by low-frequency artefacts rather than genuine non-BBH signal morphology.

2. GW191127

We then consider GW191127 and find the likelihood function to peak for a compactness $C \sim 0.35$ ($\log \mathcal{L}^{C=0.5} = 33.69$ and $\log \mathcal{L}^{C=0.35} = 48.06$) in Bayesian analysis, with a residual contrast of 0.037 between PhenomDECO and PhenomXPHM. This is comparable to what we find for events in which the likelihood peaks near $C \sim 0.5$ (see Table I). Taken in isolation, this might suggest that a moderately reduced compactness provides an equally good description of the data. However, for this event the maximum-likelihood (maxL) total mass and mass ratio are shifted relative to the BBH analysis, as expected from the degeneracies discussed in Ref. [31]. In other words, the improved agreement is achieved only by compensating the modified merger morphology with biased intrinsic parameters as shown in Table II. This highlights that a clean

TABLE II: Total mass and mass ratio corresponding to the maximum likelihood obtained in Bayesian analysis with PhenomDECO and PhenomXPHM for GW191127.

Waveform	$\max(\log \mathcal{L})$	$M^{\max\text{L}}$	$q^{\max\text{L}}$
PhenomDECO	48.06	$52.5 M_{\odot}$	0.24
PhenomXPHM	45.38	$72.1 M_{\odot}$	0.77

subtraction is not sufficient to support an exotic interpretation and supports our conservative requirement that $C = 0.5$ lie outside the 90% CI of the compactness posterior before treating an event as a candidate departure from the BBH hypothesis.

3. GW200219

Finally, we consider GW200219, which was reported with the largest residual SNR and, more importantly, the

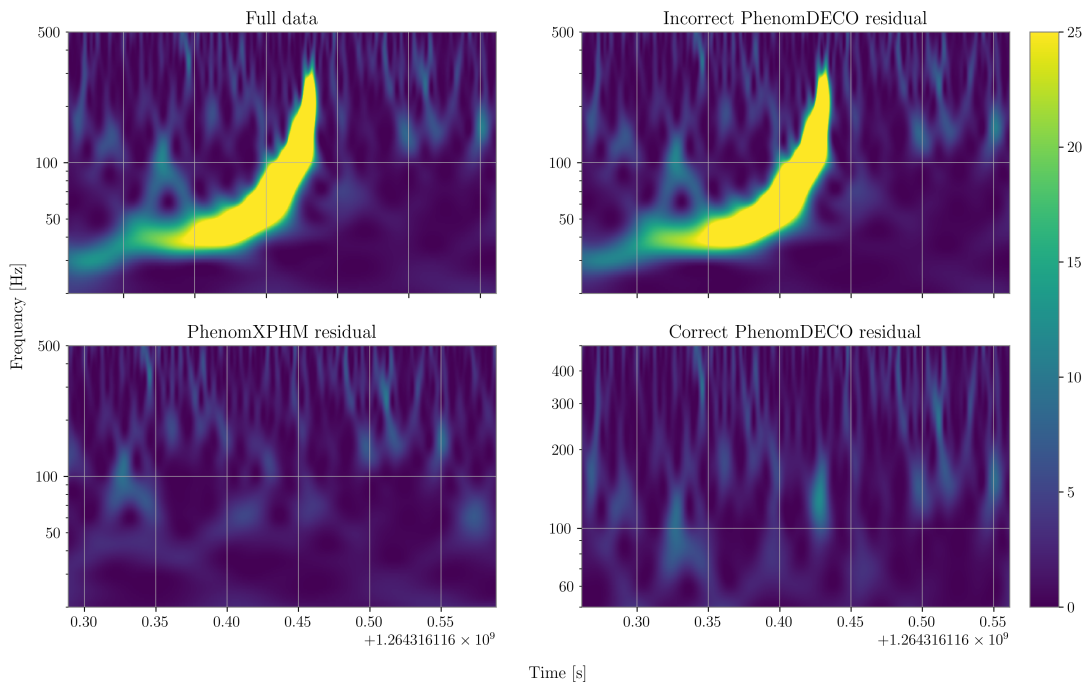


FIG. 13: Top left: spectrogram of the publicly available deglitched strain data for GW200129. Top right: residual spectrogram obtained after subtracting the maximum-likelihood PhenomDECO waveform from the analysis that favors $C \sim 0.15$. Bottom left: residual spectrogram obtained after subtracting the maximum-likelihood BBH waveform. Bottom right: residual spectrogram obtained after subtracting the maximum-likelihood PhenomDECO waveform from the analysis using a 50 Hz lower frequency cutoff for Livingston.

poorest fit by the GR template in LVK GWTC-3 tests of GR analysis ($FF_{90} = 0.74$ see table III in [30] for details). Our analysis yields a compactness posterior consistent with the BBH expectation, with a maxL value of $C^{\text{maxL}} \sim 0.482$, and a residual contrast of 0.077, comparable to events in our sample where likelihood peaks at $C \sim 0.5$. Left panel on Fig. 14 shows the distribution of normalized energies in the spectrograms for the Livingston strain, detector noise and residuals after subtraction with PhenomXPHM and PhenomDECO [76]. For comparison, right panel on Fig. 14 shows the distribution of normalized energies for GW190408_181802 in which the BBH template provides a much cleaner subtraction ($FF_{90} = 0.88$). The residual distributions in this case lie noticeably closer to the detector-noise distribution, which is obtained from the spectrogram of the detector data excluding the signal.

Notably, the residual contrast does not increase drastically for nearby lower-likelihood samples, for example at $C = 0.4$, $\Delta_{\text{res}} = 0.072$. By contrast, if the compactness is artificially reduced to $C \sim 0.3$ (which has no support in the posterior probability distribution of the compactness parameter) while the remaining source parameters are held fixed at their maxL values, the subtraction deteriorates visibly with a residual contrast of $\Delta_{\text{res}} = 0.72$.

It is worth emphasizing that the residual contrast is primarily a measure of whether the two waveform models leave comparable residual structure, in which case it is expected to be close to zero. It is not, however, a quantitative statistic for comparing subtraction quality across different events, since its normalization is set by the total strain spectrogram energy in a given detector and therefore varies from event

to event. Its usefulness instead lies in interpreting, on an event-by-event basis, whether anomalous residual structure is better accounted for by the specific waveform deformation encoded by PhenomDECO. In this sense, it is complementary to the LVK residual analysis, which identifies events for which the best-fit BBH waveform leaves anomalous residual power, whereas the PhenomDECO residual analysis tests whether such an anomaly is consistent with a physically targeted deformation of the merger morphology. At least in the case of GW200219, we find that, despite the moderately poor fit of the GR template, this specific non-BBH deformation is not favoured.

We do not apply this diagnostic to GW231123 here, since its unusually complex time–frequency morphology would require a more tailored treatment than our simple thresholded residual-contrast statistic (cf. Fig. 1 of Ref. [12]).

VI. CONCLUSION

BBHs are the standard interpretation for the majority of compact binary mergers observed in GWs, but in practice this classification is driven largely by the inferred component masses inferred from data with waveform models that describe BBHs in GR. There are existing tests that probe the nature of compact objects by tracking deviations either in the inspiral, through tidal and spin-induced finite-size effects, or in the remnant, through ringdown consistency and post-merger searches. The merger morphology itself provides a complementary diagnostic, especially for high-mass or otherwise unusual systems in which much of the

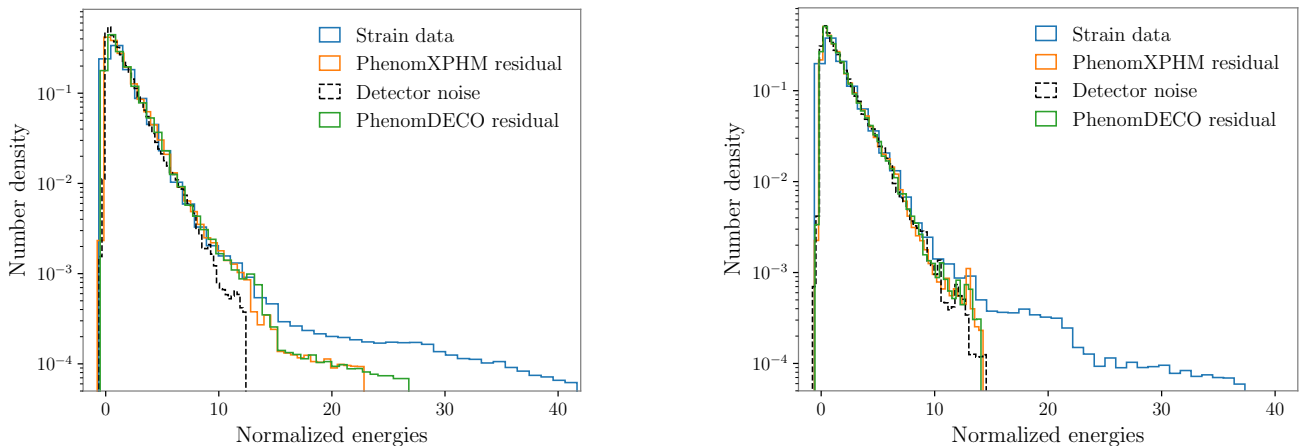


FIG. 14: Normalized energy distributions for two events. Left panel shows GW200219, which was identified in LVK tests of GR as having relatively large residual power after subtraction of the best-fit GR waveform. Right panel shows GW190408 as a comparison case with a cleaner BBH subtraction. In both panels, the PhenomXPHM and PhenomDECO residual distributions are compared with the original strain data and with the detector-noise distribution estimated from data excluding the signal. The residuals for GW190408 lie closer to the detector-noise distribution than those for GW200219, illustrating the difference between a poorer and a cleaner BBH subtraction.

observed signal power lies near merger. This is the regime probed by PhenomDECO.

In this work, we have presented the first systematic measurement of the effective compactness parameter inferred by PhenomDECO across a large sample of gravitational-wave events. Using the GWTC-3 BBH population as a benchmark, we find that most events are consistent with the BBH expectation, with compactness posteriors peaked near or including $C = 0.5$. We also identify two recurring classes of non-standard posterior behaviour: events with support at $C > 0.5$, which we interpret as BBH-like within the present parametrization rather than as evidence for a physical compactness above the black-hole value, and events with sharp low-compactness modes near $C \approx 0.15$. The latter are accompanied by additional signs of unreliable inference, including poor recovery of the chirp mass, anomalously low single-detector SNRs, and weak localization of the merger time. They are also not robust under changes to the low-frequency analysis cutoff: in all such GWTC-3 cases, raising the Livingston cutoff removes the low-compactness mode and restores BBH-like compactness. This population-level behaviour is summarized in Fig. 8, where the compactness posteriors are shown on a common set of bins. After the Livingston reanalysis, the events that initially showed sharp support near $C \approx 0.15$ no longer stand out as low-compactness outliers.

GW231123 also displays a low-compactness mode when analyzed from 20 Hz, but its behavior is qualitatively different from the low- C cases identified in the GWTC-3 benchmark. In the GWTC-3 events, the low- C mode was removed by raising the low-frequency cutoff in Livingston alone, indicating a detector-specific low-frequency artifact. For GW231123, by contrast, the low- C mode persists when the cutoff is raised in only one detector, and BBH-like compactness is recovered only when both Hanford and Livingston are analyzed above 50 Hz. This distinction makes GW231123 an outlier with respect to the empirical benchmark established here. The result does not by itself sup-

port an exotic interpretation: the event is high-mass, short-duration, and affected by known data-analysis challenges, and apparent deviations in merger morphology can arise from noise structure, waveform systematics, or missing physics in the model. However, the absence of flagged coincident data-quality issues, together with the fact that the anomaly depends on a common low-frequency cutoff across detectors, makes a purely uncorrelated detector-noise explanation less compelling than in the GWTC-3 cases. GW231123 therefore motivates targeted follow-up studies of shared low-frequency systematics, glitch mitigation, and non-CBC transient models before any non-standard astrophysical interpretation can be drawn.

Beyond the compactness-based criteria of Sec. III B, it is important to examine whether the preferred PhenomDECO solution leaves residual structure in the data that is meaningfully different from a BBH subtraction. For example, for GW191127 the likelihood peaks at $C \approx 0.35$, and the residual contrast between the maximum-likelihood PhenomDECO and BBH subtractions is comparable to that found in events where the likelihood instead peaks near $C \approx 0.5$. Taken alone, this could suggest that a moderately lower compactness provides an equally viable description of the data. However, the maximum-likelihood total mass and mass ratio inferred with PhenomDECO are not consistent with those obtained in the BBH analysis, indicating that the lower-compactness solution is accompanied by compensating shifts in the intrinsic parameters rather than a cleanly isolated change in merger morphology. If $C = 0.5$ were confidently excluded this event would have been interesting for follow-up but in the present analysis the broad compactness posterior prevents such an interpretation. This also highlights the importance of reducing these degeneracies, for example through improved PhenomDECO modelling that narrows the compactness posterior, will be essential for turning such cases into robust candidate tests of non-BBH merger morphology.

GW200219 provides a complementary example of the

role of residual diagnostics. This event was identified in the LVK tests of GR as having unusually large residual power after subtraction of the best-fit GR waveform, indicating that the GR template was a poor description of the data. In those tests, the residual analysis searches for coherent excess power remaining in the stretch of data analysed after the CBC signal has been removed, thereby asking whether the data contain structure not captured by the best-fit BBH model. The residual diagnostic used here asks a more targeted question: whether the residual power is better accounted for by the specific parametric deformation of the late-inspiral to merger morphology introduced by PhenomDECO. For GW200219, we find a compactness posterior consistent with the BBH expectation and the residual histograms to be consistent with that of detector noise. Thus, although GW200219 shows anomalous residual power in a generic residual test, that residual structure is not explained by the modification to merger morphology considered here. This highlights the complementarity of the two residual approaches: LVK-style residual tests can identify events with excess coherent power, while model-based residual analysis can test whether such excess power is consistent with a particular non-BBH modification of the merger morphology.

Across the GWTC-3 events considered here, we find no case that satisfies our robustness criteria for a non-BBH classification. Apparent low-compactness modes are removed once the detector-dependent low-frequency data treatment is varied, indicating that these features are more naturally explained by noise artefacts and inference pathologies than by genuine non-BBH merger morphology. GW231123 remains a special case: a BBH-like compactness posterior is recovered only after applying a higher low-frequency cutoff in both detectors, but controlled high-mass and precessing BBH injections suggest that neither high total mass nor spin precession alone drives PhenomDECO toward spurious low compactness. Overall, these results show that low-frequency data treatment is crucial before attributing apparent deviations from BBH expectations to exotic physics.

Taken together, these results establish effective compactness as a diagnostic of merger morphology and, through it, as a consistency check of the BBH interpretation. By applying PhenomDECO across a broad event sample, identifying recurring posterior morphologies, and testing the stability of apparent low- C support under detector-dependent low-frequency cutoffs, we have established a practical robustness framework for interpreting compactness inference on real GW data. Future work should focus on improving the PhenomDECO model in ways that reduce parameter biases and sharpen compactness measurements across events. This includes extending the waveform beyond its current amplitude-only aligned-spin implementation and incorporating relevant finite-size effects, such as tidal contributions, where appropriate. As the GW catalog continues to grow, the identification of compact binaries will become an increasingly empirical problem. A scalable method such as PhenomDECO, which can be applied broadly across events as a first-pass BBH-consistency test, provides a practical way to identify systems that merit more targeted follow-up.

VII. ACKNOWLEDGEMENTS

We thank N. V. Krishnendu for comments during the LIGO–Virgo–KAGRA internal review. SG thanks Erik Katsavounidis for valuable feedback on the presentation of residuals, and Salvatore Vitale and Gabriela González for insightful discussions. SG and FO acknowledges support from the Max Planck Society and CH thanks the University of Portsmouth for support through the Dennis Sciama Fellowship. MH was supported by Science and Technology Facilities Council (STFC) grant ST/V00154X/1. We are grateful for computational resources provided by the LIGO Laboratory, supported by the National Science Foundation Grants PHY-0757058 and PHY-0823459, and the SCIAM high performance computing cluster supported by the Institute of Cosmology and Gravitation (ICG) and the University of Portsmouth.

This research has made use of data or software obtained from the Gravitational Wave Open Science Center (gwosc.org), a service of the LIGO Scientific Collaboration, the Virgo Collaboration, and KAGRA. This material is based upon work supported by NSF’s LIGO Laboratory which is a major facility fully funded by the National Science Foundation, as well as the Science and Technology Facilities Council (STFC) of the United Kingdom, the Max-Planck-Society (MPS), and the State of Niedersachsen/Germany for support of the construction of Advanced LIGO and construction and operation of the GEO600 detector. Additional support for Advanced LIGO was provided by the Australian Research Council. Virgo is funded, through the European Gravitational Observatory (EGO), by the French Centre National de Recherche Scientifique (CNRS), the Italian Istituto Nazionale di Fisica Nucleare (INFN) and the Dutch Nikhef, with contributions by institutions from Belgium, Germany, Greece, Hungary, Ireland, Japan, Monaco, Poland, Portugal, Spain. KAGRA is supported by Ministry of Education, Culture, Sports, Science and Technology (MEXT), Japan Society for the Promotion of Science (JSPS) in Japan; National Research Foundation (NRF) and Ministry of Science and ICT (MSIT) in Korea; Academia Sinica (AS) and National Science and Technology Council (NSTC) in Taiwan. This material is based upon work supported by NSF’s LIGO Laboratory which is a major facility fully funded by the National Science Foundation. For the purpose of open access, the author(s) has applied a Creative Commons Attribution (CC BY) licence to any Author Accepted Manuscript version arising.

Appendix A: Events table

TABLE III: Median values of source-frame total mass M , the mass ratio $q \equiv m_2/m_1 \leq 1$, and the network matched-filter SNR from Refs. [77, 78] for the events analyzed in this work, with the index used in figure 8.

Index	Event	$M [M_\odot]$	q	ρ_{network}
0	GW150914	64.5	0.87	26.0
1	GW151012	38.8	0.55	9.3
2	GW151226	21.7	0.53	12.7
3	GW170104	49.6	0.72	13.8
4	GW170608	18.5	0.74	15.3
5	GW170729	84.4	0.55	10.7
6	GW170809	58.5	0.71	12.8
7	GW170814	56.0	0.81	17.7
8	GW170818	62.5	0.79	12.0
9	GW170823	67.0	0.76	12.2
10	GW190408_181802	34.3	0.64	14.6
11	GW190412	36.8	0.32	19.8
12	GW190413_052954	58.0	0.72	9.0
13	GW190413_134308	81.3	0.59	10.6
14	GW190421_213856	73.6	0.76	10.7
15	GW190503_185404	69.4	0.69	12.2
16	GW190512_180714	35.8	0.54	12.7
17	GW190513_205428	54.4	0.51	12.5
18	GW190514_065416	69.3	0.69	8.0
19	GW190517_055101	64.1	0.61	10.8
20	GW190519_153544	105.6	0.63	15.9
21	GW190521	153.1	0.58	14.3
22	GW190521_074359	76.3	0.77	25.9
23	GW190527_092055	58.1	0.62	8.0
24	GW190602_175927	115.6	0.62	13.2
25	GW190620_030421	92.7	0.60	12.1
26	GW190630_185205	59.4	0.68	16.4
27	GW190701_203306	94.3	0.75	11.2
28	GW190706_222641	112.6	0.67	13.4
29	GW190707_093326	20.1	0.65	13.1
30	GW190708_232457	31.4	0.59	13.4
31	GW190719_215514	57.2	0.54	7.9
32	GW190720_000836	21.8	0.53	10.9
33	GW190725_174728	18.3	0.53	9.1
34	GW190727_060333	68.8	0.78	11.7

Index	Event	$M [M_\odot]$	q	ρ_{network}
35	GW190728_064510	20.7	0.64	13.1
36	GW190731_140936	70.7	0.69	8.8
37	GW190803_022701	65.0	0.73	9.3
38	GW190805_211137	76.7	0.66	8.1
39	GW190828_063405	57.2	0.81	16.5
40	GW190828_065509	34.3	0.44	10.2
41	GW190910_112807	78.0	0.78	14.5
42	GW190915_235702	57.2	0.75	13.1
43	GW190924_021846	13.9	0.58	12.0
44	GW190925_232845	36.7	0.75	9.7
45	GW190929_012149	93.3	0.40	9.7
46	GW190930_133541	21.2	0.49	9.7
47	GW191103_012549	20.0	0.67	8.9
48	GW191105_143521	18.5	0.66	9.7
49	GW191109_010717	112.0	0.72	17.3
50	GW191127_050227	80.0	0.45	9.2
51	GW191129_134029	17.5	0.63	13.1
52	GW191204_171526	20.2	0.69	17.5
53	GW191215_223052	43.3	0.73	11.2
54	GW191216_213338	19.8	0.64	18.6
55	GW191222_033537	79.0	0.77	12.5
56	GW191230_180458	86.0	0.75	10.4
57	GW200112_155838	63.9	0.79	19.8
58	GW200128_022011	75.0	0.77	11.0
59	GW200129_065458	63.4	0.84	26.8
60	GW200202_154313	17.6	0.72	10.8
61	GW200208_130117	65.4	0.72	10.8
62	GW200209_085452	62.6	0.76	9.6
63	GW200219_094415	65.0	0.74	10.7
64	GW200224_222234	72.2	0.81	20.0
65	GW200225_060421	33.5	0.73	12.5
66	GW200302_015811	57.8	0.53	10.8
67	GW200311_115853	61.9	0.81	17.8
68	GW200316_215756	21.2	0.60	10.3

- [1] R. Abbott *et al.* (LIGO Scientific Collaboration and Virgo Collaboration and KAGRA Collaboration), GWTC-3: Compact binary coalescences observed by LIGO and Virgo during the second part of the third observing run, *Physical Review X* **13**, 041039 (2023), [arXiv:2111.03606 \[gr-qc\]](#).
- [2] A. H. Nitz, S. Kumar, Y.-F. Wang, S. Kasta, S. Wu, M. Schäfer, R. Dhurkunde, and C. D. Capano, 4-ogc: Catalog of gravitational waves from compact binary mergers, *The Astrophysical Journal* **946**, 59 (2023).
- [3] T. Venumadhav, B. Zackay, J. Roulet, L. Dai, and M. Zaldarriaga, New binary black hole mergers in the second observing run of advanced ligo and advanced virgo, *Phys. Rev. D* **101**, 083030 (2020).
- [4] S. Olsen, T. Venumadhav, J. Mushkin, J. Roulet, B. Zackay, and M. Zaldarriaga, New binary black hole mergers in the LIGO-Virgo O3a data, *Phys. Rev. D* **106**, 043009 (2022), [arXiv:2201.02252 \[astro-ph.HE\]](#).
- [5] A. K. Mehta, S. Olsen, D. Wadekar, J. Roulet, T. Venumadhav, J. Mushkin, B. Zackay, and M. Zaldarriaga, New binary black hole mergers in the LIGO-Virgo O3b data, *Phys. Rev. D* **111**, 024049 (2025), [arXiv:2311.06061 \[gr-qc\]](#).
- [6] A. G. Abac *et al.* (LIGO Scientific Collaboration and Virgo Collaboration and KAGRA Collaboration), GWTC-4.0: Updating the gravitational-wave transient catalog with observations from the first part of the fourth LIGO-Virgo-KAGRA observing run [10.48550/arXiv.2508.18082](#) (2025), [arXiv:2508.18082 \[gr-qc\]](#).
- [7] N. Abac *et al.* (LIGO Scientific, VIRGO, KAGRA), GWTC-5.0: An Introduction to Version 5.0 of the Gravitational-Wave Transient Catalog, (2026), [arXiv:2605.27223 \[gr-qc\]](#).
- [8] GWTC-5.0: Population Properties of Merging Compact Binaries, (2026), [arXiv:2605.27226 \[astro-ph.HE\]](#).
- [9] R. Abbott *et al.* (LIGO Scientific Collaboration and Virgo Collaboration), GW190814: Gravitational waves from the coalescence of a 23 solar mass black hole with a 2.6 solar mass compact object, *The Astrophysical Journal Letters* **896**, L44 (2020), [arXiv:2006.12611 \[astro-ph.HE\]](#).
- [10] A. G. Abac *et al.* (LIGO Scientific Collaboration and Virgo Collaboration and KAGRA Collaboration), Observation of gravitational waves from the coalescence of a 2.5–4.5 m_\odot compact object and a neutron star, *The Astrophysical Journal Letters* **970**, L34 (2024), [arXiv:2404.04248 \[astro-ph.HE\]](#).
- [11] R. Abbott *et al.* (LIGO Scientific Collaboration and Virgo Collaboration), GW190521: A binary black hole merger with a total mass of 150 m_\odot , *Physical Review Letters* **125**, 101102 (2020), [arXiv:2009.01075 \[gr-qc\]](#).

- [12] A. G. Abac *et al.* (LIGO Scientific, VIRGO, KAGRA), GW231123: A Binary Black Hole Merger with Total Mass 190–265 M_{\odot} , *Astrophys. J. Lett.* **993**, L25 (2025), [arXiv:2507.08219 \[astro-ph.HE\]](#).
- [13] P. Ajith *et al.*, Phenomenological template family for black-hole coalescence waveforms, *Class. Quant. Grav.* **24**, S689 (2007), [arXiv:0704.3764 \[gr-qc\]](#).
- [14] P. Ajith *et al.*, Inspiral-merger-ringdown waveforms for black-hole binaries with non-precessing spins, *Phys. Rev. Lett.* **106**, 241101 (2011), [arXiv:0909.2867 \[gr-qc\]](#).
- [15] S. Khan, S. Husa, M. Hannam, F. Ohme, M. Pürrer, X. Jiménez Forteza, and A. Bohé, Frequency-domain gravitational waves from nonprecessing black-hole binaries. II. A phenomenological model for the advanced detector era, *Phys. Rev. D* **93**, 044007 (2016), [arXiv:1508.07253 \[gr-qc\]](#).
- [16] S. Husa, S. Khan, M. Hannam, M. Pürrer, F. Ohme, X. Jiménez Forteza, and A. Bohé, Frequency-domain gravitational waves from nonprecessing black-hole binaries. I. New numerical waveforms and anatomy of the signal, *Phys. Rev. D* **93**, 044006 (2016), [arXiv:1508.07250 \[gr-qc\]](#).
- [17] M. Hannam, P. Schmidt, A. Bohé, L. Haegel, S. Husa, F. Ohme, G. Pratten, and M. Pürrer, Simple Model of Complete Precessing Black-Hole-Binary Gravitational Waveforms, *Phys. Rev. Lett.* **113**, 151101 (2014), [arXiv:1308.3271 \[gr-qc\]](#).
- [18] J. E. Thompson, E. Hamilton, L. London, S. Ghosh, P. Koltidou, C. Hoy, and M. Hannam, PhenomXO4a: a phenomenological gravitational-wave model for precessing black-hole binaries with higher multipoles and asymmetries, *Phys. Rev. D* **109**, 063012 (2024), [arXiv:2312.10025 \[gr-qc\]](#).
- [19] M. Colleoni, F. A. R. Vidal, C. García-Quirós, S. Akçay, and S. Bera, Fast frequency-domain gravitational waveforms for precessing binaries with a new twist, *Phys. Rev. D* **111**, 104019 (2025), [arXiv:2412.16721 \[gr-qc\]](#).
- [20] E. Hamilton *et al.*, Improved gravitational wave model linking precessing inspirals and numerical-relativity-calibrated merger-ringdown, *Phys. Rev. D* **113**, 084055 (2026), [arXiv:2507.02604 \[gr-qc\]](#).
- [21] S. Ghosh, P. Koltidou, and M. Hannam, First frequency-domain phenomenological model of the multipole asymmetry in gravitational-wave signals from binary-black-hole coalescence, *Phys. Rev. D* **109**, 024061 (2024), [arXiv:2310.16980 \[gr-qc\]](#).
- [22] A. Buonanno and T. Damour, Effective one-body approach to general relativistic two-body dynamics, *Phys. Rev. D* **59**, 084006 (1999), [arXiv:gr-qc/9811091](#).
- [23] A. Buonanno and T. Damour, Transition from inspiral to plunge in binary black hole coalescences, *Phys. Rev. D* **62**, 064015 (2000), [arXiv:gr-qc/0001013](#).
- [24] A. Taracchini *et al.*, Effective-one-body model for black-hole binaries with generic mass ratios and spins, *Phys. Rev. D* **89**, 061502 (2014), [arXiv:1311.2544 \[gr-qc\]](#).
- [25] A. Buonanno, Y. Chen, and T. Damour, Transition from inspiral to plunge in precessing binaries of spinning black holes, *Phys. Rev. D* **74**, 104005 (2006), [arXiv:gr-qc/0508067](#).
- [26] A. Ramos-Buades, A. Buonanno, H. Estellés, M. Khalil, D. P. Mihaylov, S. Ossokine, L. Pompili, and M. Shiferaw, Next generation of accurate and efficient multipolar precessing-spin effective-one-body waveforms for binary black holes, *Phys. Rev. D* **108**, 124037 (2023), [arXiv:2303.18046 \[gr-qc\]](#).
- [27] H. Estellés, A. Buonanno, R. Enficiaud, C. Foo, and L. Pompili, Adding equatorial-asymmetric effects for spin-precessing binaries into the seobnr5phm waveform model, *Phys. Rev. D* **113**, 044049 (2026), [arXiv:2506.19911 \[gr-qc\]](#).
- [28] T. Evstafyeva, U. Sperhake, I. Romero-Shaw, and M. Agathos, Gravitational-wave data analysis with high-precision numerical relativity simulations of boson star mergers, (2024), [arXiv:2406.02715 \[gr-qc\]](#).
- [29] T. Evstafyeva, A. Seifert, U. Sperhake, C. J. Moore, and T. Jain, Lessons from binary dynamics of inspiralling equal-mass boson-star mergers, (2026), [arXiv:2604.25582 \[gr-qc\]](#).
- [30] R. Abbott *et al.* (LIGO Scientific, VIRGO, KAGRA), Tests of General Relativity with GWTC-3, *Phys. Rev. D* **112**, 084080 (2025), [arXiv:2112.06861 \[gr-qc\]](#).
- [31] S. Ghosh and M. Hannam, Identification of exotic compact binaries with gravitational waves: A phenomenological approach, *Phys. Rev. D* **112**, 104017 (2025), [arXiv:2505.16380 \[gr-qc\]](#).
- [32] S. Ghosh, C. Hoy, M. Hannam, and F. Ohme, Establishing Compactness as a Population Observable in Gravitational-Wave Astronomy, (2026), [arXiv:2606.31364 \[gr-qc\]](#).
- [33] J. Aasi *et al.* (LIGO Scientific), Advanced LIGO, *Class. Quant. Grav.* **32**, 074001 (2015), [arXiv:1411.4547 \[gr-qc\]](#).
- [34] A. Buikema *et al.* (aLIGO), Sensitivity and performance of the Advanced LIGO detectors in the third observing run, *Phys. Rev. D* **102**, 062003 (2020), [arXiv:2008.01301 \[astro-ph.IM\]](#).
- [35] M. Tse *et al.*, Quantum-Enhanced Advanced LIGO Detectors in the Era of Gravitational-Wave Astronomy, *Phys. Rev. Lett.* **123**, 231107 (2019).
- [36] F. Acernese *et al.* (VIRGO), Advanced Virgo: a second-generation interferometric gravitational wave detector, *Class. Quant. Grav.* **32**, 024001 (2015), [arXiv:1408.3978 \[gr-qc\]](#).
- [37] F. Acernese *et al.* (Virgo), Increasing the Astrophysical Reach of the Advanced Virgo Detector via the Application of Squeezed Vacuum States of Light, *Phys. Rev. Lett.* **123**, 231108 (2019).
- [38] F. Acernese *et al.* (Virgo), Virgo detector characterization and data quality: results from the O3 run, *Class. Quant. Grav.* **40**, 185006 (2023), [arXiv:2210.15633 \[gr-qc\]](#).
- [39] K. Somiya (KAGRA), Detector configuration of KAGRA: The Japanese cryogenic gravitational-wave detector, *Class. Quant. Grav.* **29**, 124007 (2012), [arXiv:1111.7185 \[gr-qc\]](#).
- [40] Y. Aso, Y. Michimura, K. Somiya, M. Ando, O. Miyakawa, T. Sekiguchi, D. Tatsumi, and H. Yamamoto (The KAGRA Collaboration), Interferometer design of the kagra gravitational wave detector, *Phys. Rev. D* **88**, 043007 (2013).
- [41] T. Akutsu *et al.* (KAGRA), Overview of KAGRA: Detector design and construction history, *PTEP* **2021**, 05A101 (2021), [arXiv:2005.05574 \[physics.ins-det\]](#).
- [42] N. V. Krishnendu, K. G. Arun, and C. K. Mishra, Testing the binary black hole nature of a compact binary coalescence, *Phys. Rev. Lett.* **119**, 091101 (2017), [arXiv:1701.06318 \[gr-qc\]](#).
- [43] N. V. Krishnendu, M. Saleem, A. Samajdar, K. G. Arun, W. Del Pozzo, and C. K. Mishra, Constraints on the binary black hole nature of GW151226 and GW170608 from the measurement of spin-induced quadrupole moments, *Phys. Rev. D* **100**, 104019 (2019), [arXiv:1908.02247 \[gr-qc\]](#).
- [44] N. V. Krishnendu, F. Ohme, and K. G. Arun, Testing the nature of compact objects in the lower mass gap using gravitational wave observations (2025), [arXiv:2509.10420 \[astro-ph.HE\]](#).
- [45] O. Dreyer, B. J. Kelly, B. Krishnan, L. S. Finn, D. Garrison, and R. Lopez-Aleman, Black hole spectroscopy: Testing general relativity through gravitational wave observations, *Class. Quant. Grav.* **21**, 787 (2004), [arXiv:gr-qc/0309007](#).
- [46] E. Berti, V. Cardoso, and C. M. Will, On gravitational-wave spectroscopy of massive black holes with the space interferometer LISA, *Phys. Rev. D* **73**, 064030 (2006), [arXiv:gr-qc/0512160](#).
- [47] N. Uchikata, H. Nakano, T. Narikawa, N. Sago, H. Tagoshi, and T. Tanaka, Searching for black hole echoes from the LIGO-Virgo Catalog GWTC-1, *Phys. Rev. D* **100**, 062006 (2019), [arXiv:1906.00838 \[gr-qc\]](#).

- [48] N. Uchikata, T. Narikawa, H. Nakano, N. Sago, H. Tagoshi, and T. Tanaka, Searching for gravitational wave echoes from black hole binary events in the third observing run of LIGO, Virgo, and KAGRA collaborations, *Phys. Rev. D* **108**, 104040 (2023), arXiv:2309.01894 [gr-qc].
- [49] S. A. Hughes and K. Menou, Golden binaries for LISA: Robust probes of strong-field gravity, *Astrophys. J.* **623**, 689 (2005), arXiv:astro-ph/0410148.
- [50] A. Ghosh *et al.*, Testing general relativity using golden black-hole binaries, *Phys. Rev. D* **94**, 021101 (2016), arXiv:1602.02453 [gr-qc].
- [51] C. Palenzuela, I. Olabarrieta, L. Lehner, and S. L. Liebling, Head-on collisions of boson stars, *Phys. Rev. D* **75**, 064005 (2007), arXiv:gr-qc/0612067.
- [52] C. Palenzuela, L. Lehner, and S. L. Liebling, Orbital Dynamics of Binary Boson Star Systems, *Phys. Rev. D* **77**, 044036 (2008), arXiv:0706.2435 [gr-qc].
- [53] T. Dietrich, S. Ossokine, and K. Clough, Full 3D numerical relativity simulations of neutron star–boson star collisions with BAM, *Class. Quant. Grav.* **36**, 025002 (2019), arXiv:1807.06959 [gr-qc].
- [54] K. Clough, T. Dietrich, and J. C. Niemeyer, Axion star collisions with black holes and neutron stars in full 3D numerical relativity, *Phys. Rev. D* **98**, 083020 (2018), arXiv:1808.04668 [gr-qc].
- [55] N. Siemonsen and W. E. East, Binary boson stars: Merger dynamics and formation of rotating remnant stars, *Phys. Rev. D* **107**, 124018 (2023), arXiv:2302.06627 [gr-qc].
- [56] G. Pratten *et al.*, Computationally efficient models for the dominant and subdominant harmonic modes of precessing binary black holes, *Phys. Rev. D* **103**, 104056 (2021), arXiv:2004.06503 [gr-qc].
- [57] S. Hild *et al.*, Sensitivity Studies for Third-Generation Gravitational Wave Observatories, *Class. Quant. Grav.* **28**, 094013 (2011), arXiv:1012.0908 [gr-qc].
- [58] J. S. Speagle, dynesty: a dynamic nested sampling package for estimating Bayesian posteriors and evidences, *Mon. Not. Roy. Astron. Soc.* **493**, 3132 (2020), arXiv:1904.02180 [astro-ph.IM].
- [59] G. Ashton *et al.*, BILBY: A user-friendly Bayesian inference library for gravitational-wave astronomy, *Astrophys. J. Suppl.* **241**, 27 (2019), arXiv:1811.02042 [astro-ph.IM].
- [60] I. M. Romero-Shaw *et al.*, Bayesian inference for compact binary coalescences with bilby: validation and application to the first LIGO–Virgo gravitational-wave transient catalogue, *Mon. Not. Roy. Astron. Soc.* **499**, 3295 (2020), arXiv:2006.00714 [astro-ph.IM].
- [61] T. Dietrich, D. Radice, S. Bernuzzi, F. Zappa, A. Perego, B. Brügmann, S. V. Chaurasia, R. Dudi, W. Tichy, and M. Ujevic, CoRe database of binary neutron star merger waveforms, *Class. Quant. Grav.* **35**, 24LT01 (2018), arXiv:1806.01625 [gr-qc].
- [62] R. Dudi, F. Pannarale, T. Dietrich, M. Hannam, S. Bernuzzi, F. Ohme, and B. Brügmann, Relevance of tidal effects and post-merger dynamics for binary neutron star parameter estimation, *Phys. Rev. D* **98**, 084061 (2018), arXiv:1808.09749 [gr-qc].
- [63] M. Hannam *et al.*, General-relativistic precession in a black-hole binary, *Nature* **610**, 652 (2022), arXiv:2112.11300 [gr-qc].
- [64] E. Payne, S. Hourihane, J. Golomb, R. Udall, R. Udall, D. Davis, and K. Chatziioannou, Curious case of GW200129: Interplay between spin-precession inference and data-quality issues, *Phys. Rev. D* **106**, 104017 (2022), arXiv:2206.11932 [gr-qc].
- [65] D. Nandi, A. Effler, S. Soni, T. A. Ferreira, R. Schofield, H. Pham, T. O’Hanlon, V. V. Frolov, and G. González, Scattered light noise at LIGO Livingston observatory during o4 (2026), arXiv:2605.14143 [astro-ph.IM].
- [66] A. G. Abac *et al.* (LIGO Scientific, Virgo, KAGRA), GW250114: Testing Hawking’s Area Law and the Kerr Nature of Black Holes, *Phys. Rev. Lett.* **135**, 111403 (2025), arXiv:2509.08054 [gr-qc].
- [67] R. Abbott *et al.* (LIGO Scientific, Virgo), GW190412: Observation of a Binary-Black-Hole Coalescence with Asymmetric Masses, *Phys. Rev. D* **102**, 043015 (2020), arXiv:2004.08342 [astro-ph.HE].
- [68] A. G. Abac *et al.* (LIGO Scientific, Virgo, KAGRA), Black Hole Spectroscopy and Tests of General Relativity with GW250114, *Phys. Rev. Lett.* **136**, 041403 (2026), arXiv:2509.08099 [gr-qc].
- [69] A. Akyüz, A. Correia, J. Garofalo, K. Kacanja, L. Roy, K. Soni, H. Tan, V. J. Y. A. H. Nitz, and C. D. Capano, Potential science with GW250114 – the loudest binary black hole merger detected to date, (2025), arXiv:2507.08789 [gr-qc].
- [70] L. Grimaldi, E. Maggio, L. Pompili, and A. Buonanno, Plunge-merger-ringdown tests of general relativity with GW250114, *Phys. Rev. D* **113**, L061506 (2026), arXiv:2601.13173 [gr-qc].
- [71] S. Bini, K. Król, K. Chatziioannou, and M. Isi, The impact of waveform systematics and Gaussian noise on the interpretation of GW231123, (2026), arXiv:2601.09678 [gr-qc].
- [72] G. Dideron, S. Mukherjee, and L. Lehner, SCoRe: A New Framework to Study Unmodeled Physics from Gravitational Wave Data, *Phys. Rev. D* **107**, 104023 (2023), arXiv:2209.14321 [gr-qc].
- [73] E. Thrane and C. Talbot, An introduction to bayesian inference in gravitational-wave astronomy: Parameter estimation, model selection, and hierarchical models, *Publications of the Astronomical Society of Australia* **36**, 10.1017/pasa.2019.2 (2019).
- [74] S. Chatterji, Ph.d. thesis, massachusetts institute of technology, 2005, (2005).
- [75] D. M. Macleod, J. S. Areeda, S. B. Coughlin, T. J. Massinger, and A. L. Urban, Gwpy: A python package for gravitational-wave astrophysics, *SoftwareX* **13**, 100657 (2021).
- [76] D. Liang, N. Dai, and Y. Yang, Residual test for the third gravitational-wave transient catalog, *JCAP* **04**, 022, arXiv:2509.14924 [gr-qc].
- [77] R. Abbott *et al.* (LIGO Scientific Collaboration and Virgo Collaboration and KAGRA Collaboration), GWTC-2.1: Deep Extended Catalog of Compact Binary Coalescences Observed by LIGO and Virgo During the First Half of the Third Observing Run, *Phys. Rev. D* **109**, 022001 (2024), arXiv:2108.01045 [gr-qc].
- [78] R. Abbott *et al.* (LIGO Scientific Collaboration and Virgo Collaboration and KAGRA Collaboration), GWTC-3: Compact Binary Coalescences Observed by LIGO and Virgo During the Second Part of the Third Observing Run, *Phys. Rev. X* **13**, 041039 (2023), arXiv:2111.03606 [gr-qc].